National Synchrotron Light Source II

# NSLS-II Beamline Report for SAC Review of Beamlines

## Beamline: *X-ray Powder Diffraction* (*XPD, 28-ID-2*)

Date: September 10, 2018
Author: E. Dooryhee

U.S. DEPARTMENT OF ENERGY | Office of Science
BROOKHAVEN NATIONAL LABORATORY | National Synchrotron Light Source II

1 - Introduction ..... 5
2 - Beamline Overview ..... 5
2.1 - General Description ..... 5
2.2 – Beamline Capabilities ..... 7
2.2.1 - Endstation 1 ..... 8
2.2.2 - Endstation 2 ..... 8
2.3 – Performance and data quality ..... 8
2.4 - Software ..... 9
3 - Scientific Program ..... 10
4 - Productivity and Impact ..... 12
5 - Vision for Next Five Years ..... 15
5.1 - Battery and Energy Storage ..... 15
5.2 – Advanced Manufacturing ..... 16
5.3 – In Situ Synthesis ..... 16
5.4 – Enhanced Capabilities ..... 16
5.5 – From High-Throughput Science to Materials Design ..... 18
5.6 – Long Duration Experiments ..... 20
5.7 - Instrumental Development ..... 20
5.7.1 – Enhanced Space Resolution ..... 20
5.7.2 - Diffraction-Tomography ..... 20
5.7.3 – High Pressure ..... 21
5.7.4 – Detectors ..... 22
5.7.5 - New Methods ..... 24
6- Beamline Self-Assessment ..... 25
6.1- Reliability of XPD Operations ..... 25
6.2 - Science Focus ..... 26
6.3 – Training ..... 26
Appendix 1 - User Science Program ..... 27
1. Chemistry (ex situ structure) ..... 27
2. Physics (ex situ structure) ..... 30
3. Battery and Energy Storage Materials. ..... 32
3.1 Structure of battery materials and relationship with electrochemical performance ..... 32
3.2 Structural transformations operando ..... 34
3.3 *in situ* synthesis of battery materials ..... 36
4. Synthesis (in situ) ..... 37
5. Materials Processing ..... 39
6. Nuclear Science ..... 40
7. Instrumentation, Detectors, Methods ..... 42
7.1 Detectors ..... 42
7.2 Methods ..... 42
7.3 Sample Environments ..... 43
8. Sorption studies ..... 43
9. Earth Science ..... 44
Appendix 2 – Beamline Staff ..... 45
Appendix 3 – Sample Environment ..... 46
Appendix 4 – User partnership ..... 49

# 1 - Introduction

28-ID-2 (XPD) operates with photon beams whose energy is fully tunable between 40keV and 70keV, with a nominal beam size of 0.5 × 0.5 $mm^2$. Hard X-rays provide the opportunity to probe high-Z or bulk samples, buried phases, and through sample cells and devices. The core mission of XPD is to observe materials under conditions that are far from equilibrium, non-ambient or non-static, *i.e.,* as a function of a process parameter like T, P, pH, reactive gases, electric or magnetic field.

XPD serves a very broad and diverse user community ranging from physics, chemistry, and materials science to earth science, environmental science and engineering science. XPD's themes of excellence are: 1) *in situ* synthesis and materials processing (*e.g.,* high temperature solid state growth, growth of colloidal nanoparticles from solution, flash sintering of ceramics/oxide materials, nucleation & growth of MOFs, or microwave-assisted synthesis) and 2) *in situ* structure evolution (*e.g*., catalysis, oxidation-reduction reactions using gases, hydrogenation reactions, gas adsorption and separation, and cycling of energy-storage devices).

XPD is strongly aligned with the NSLS-II second science priority area '*Operando Chemistry and Structural Science*', as described in the strategic plan[1]. An essential component of the XPD attractiveness and impact is the development of i) a science-driven selection of sample environments and ii) a powerful science-enabling software package – this is where opportunities for new science lie.

XPD was one of the first 7 beamlines, funded on the DOE-BES construction project of NSLS-II. Instrument Readiness Review, that marks completion of the construction project, occurred in September 2014. First Light was in November 2014 and General User operations in August 2015.

# 2 - Beamline Overview

## *2.1 - General Description*

XPD uses a 1.85T wiggler source (critical energy = 11.1 keV)[2]. The photon delivery system comprises a Double-Laue crystal Monochromator (®FMB-Oxford) with sagittal focusing and a Pt-coated long mirror (®Winlight-X) for vertical focusing. The incident wiggler white beam is aggressively filtered to mitigate the heat load on the optics, as shown in Fig. 1 (also see discussion in section 6.1). The number of filters in the white beam sets the low energy cut-off (40keV).

Optic modeling and rationale for the design of the XPD beamline can be found in the Preliminary Design Report (2010) and in the Journal of Synchrotron Radiation (2013) [xpd-1].

xpd-1 X Shi, S Ghose, E Dooryhee, Performance Calculations of the X-ray Powder Diffraction Beamline at NSLS-II, *J. Synch. Rad.*, **20**(2), 234-242 (2013).

The list of Beamline staff is given in Appendix 2.
XPD user partnership is in appendix 4.

[1] NSLS-II Strategic Plan, April 2018 at https://www.bnl.gov/ps/docs/pdf/NSLS2-Strategic-Plan.pdf
[2] NSLS-II machine parameters at https://www.bnl.gov/ps/accelerator/

**Figure 1: Wiggler White Beam Spectrum and Effect of Filtering**

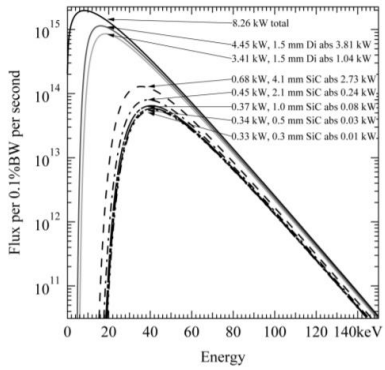


**Figure 2: XPD Beamline Layout**

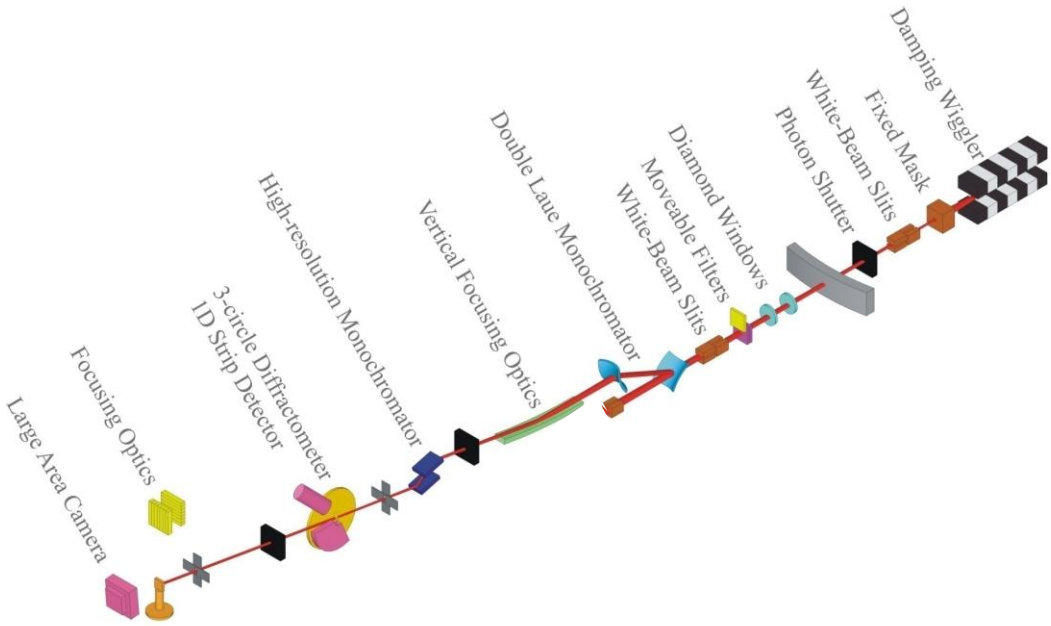

## *2.2 – Beamline Capabilities*

**Table 1: XPD Beamline Capabilities**

| | |
|---|---|
| Focused beam size (mm) | 0.60 (Ho) x 0.20 (Ve) (observed) |
| Energy range (keV) | 40-70 (tunable*) |
| X-ray Powder Diffraction (XRD, far-field)<br>"Small" Angle X-ray Scattering | Endstation 1: a large area (4k x 4k pixels) ®Perkin-Elmer a-Si detector (100µm pixel), distance to sample can be varied.<br>This detector can be occasionally used for detecting particles and precipitates smaller than 100nm<br>details here |
| Pair Distribution Function (PDF, near-field) | Endstation 1: a second large area (2k x 2k pixels) ®Perkin-Elmer a-Si detector (200µm pixel) – Qmax is 27Angstrom$^{-1}$ -<br>details here |
| Geometry | Flat plate or capillary, transmission<br>details here |
| High-throughput | robotic arm - details here |
| High Pressure diffraction | pressures >20 GPa and temperatures >2000°C |
| Diffraction-Tomography (µm) | 30 (Ho) x 20 (Ve) focused beam (calculated) |

*All XPD experiments (except for some specific cases) are conducted at 52keV (XRD) or 67keV (mostly PDF). Spectroscopic measurements (resonant or contrast diffraction) are not feasible.

Half of the work published thus far, uses the far-field detector (XRD) (Fig. 3). Users are progressively accustomed with the PDF technique and the proportion of combined XRD/PDF measurements was growing recently. XPD and PDF are essentially 2 different, and complementary, modes of the same technique. One important asset of the XPD program is to merge both modes and minimize any technical overhead by smoothly and rapidly switching between the near-field and the far-field detectors back and forth, using a 67keV beam. XPD is a truly multi-length scale probe by proposing XRD, PDF and SAXS simultaneously.

**Figure 3: Proportion of PDF and XRD work** (published work only)

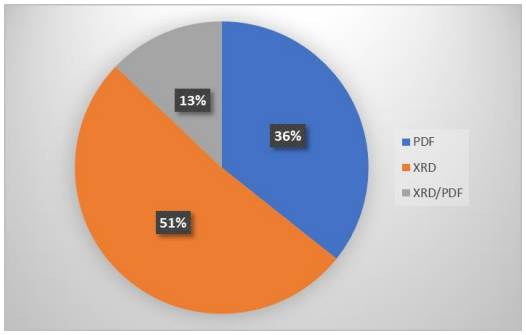


XPD offers a large variety of sample environments (commercial, user-custom or in-house systems) that include furnaces, cryostats and flow cells. The list of sample environments is given in Appendix 3.

Safety information (incl. documents[3], controls and requirements, training, etc) can be found at https://wiki-nsls2.bnl.gov/beamline28ID2/index.php/Safety

### 2.2.1 - Endstation 1

**Figure 4: experimental set-up.** (left) overview; (right) close-up that shows the detector and sample space with cameras and cryostream.

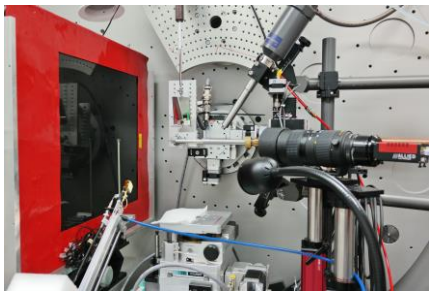

### 2.2.2 - Endstation 2

First light in endstation 2 happened in May 2017. Endstation 2 hosts 2 major pieces of equipment; i) the diffraction-tomography set-up (section 5.7.2) and ii) a multi-anvil cell (section 5.7.3). Endstation 2 has provision for large pieces of user-custom equipment, long-lead time experiments and long duration experiments (section 5.6).

## *2.3 – Performance and data quality*

Fig. 5 shows the instrumental function, grossly defined as the diffraction peak width (FWHM) vs. $2\theta$ from a NIST standard polycrystal. The high-resolution monochromator (a pseudo-channel cut Si crystal that resides in endstation 1 has the net result of decreasing the energy bandwidth contribution into peak broadening ($\Delta E/E$ is changed from ~$10^{-3}$ to ~$2 \times 10^{-4}$). But photon flux is considerably lower.

[3] Beamline Specific Training, Safety Approval Form (SAF), Radiation Safety Component List, Experimental Safety Review (ESR), Beamline System Readiness Checklist, Beamlines XPD/PDF (28-ID) Radiation Survey Procedure and Report, etc

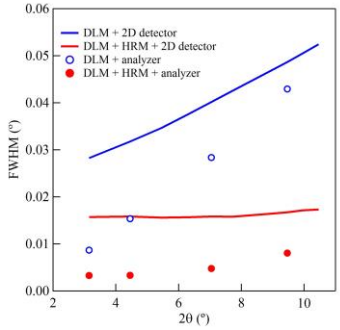


**Figure 5: Instrumental resolution of XPD.** Different combinations of Double Laue Monochromator(DLM), High Resolution Monochromator (HRM), 2D detector and post-sample analyzer crystal.

**Figure 6: comparison of XPD and APS diffraction data:** Diffraction patterns acquired at APS 11-BM-B and NSLS-II XPD on as-synthesized Gd based salt inclusion materials K9F2Gd3Si12O32 (Courtesy S. Gill, BNL)

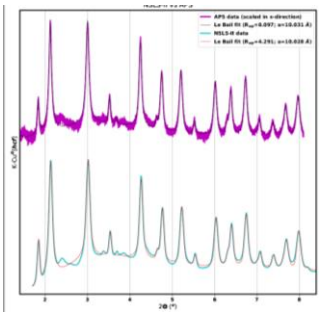

Diffraction patterns of a Prussian Blue Analogue (Cu hexacyanoferrate) acquired at APS 11-BM for 1 hour at λ=0.4127Å (top) and NSLS-II XPD for 2mn at λ=0.1867Å (bottom). When it comes to disordered or nanocrystalline structures, intrinsic diffraction peaks are broad and XPD is at its advantage.

The high flux of XPD provides a distinct advantage in time-dependent, *in situ* or operando structure tracking, and is currently limited by the detector speed (a few Hz). The high X-ray flux also helps in determining minor phases in quantitative analysis of multi-component systems with high statistics.

There were intrinsic risks and unknowns in the engineering of the XPD beamline (section 6.1). Despite these technical challenges, the beamline has not experienced any technical shutdown since the start-up of operations. XPD has had no down time, while the ring current was being ramped from 0.5mA up to 400mA (target is 500mA next year).

## *2.4 - Software*

Beamline components are controlled by EPICS. Delta Tau Geobrick LV is the standard controller for stepper motors. The user interface is implemented using Python and Control System Studio (CSS) clients operating under Linux Debian workstations with CPU and GPU clusters, and offering local and centralized data storage.

The XPD beamline uses the NSLS-II software (http://nsls-ii.github.io/) that is based on Ophyd - a python-based ("spec-like") command line interface for scanning and Bluesky - a library for experiment control and collection of scientific data and metadata (http://nsls-ii.github.io/bluesky/ ).

On top of Bluesky, XPD custom software toolkits (Python) for powder diffraction experiments are developed by S. Billinge (BNL - University of Columbia – see User Partnership in Appendix 4): http://xpdacq.github.io/. It consists in 2 parts that are fully documented on Github:

- XPD data acquisition and data management: xpdAcq
- XPD data processing and data visualization: xpdAn

Comprehensive information and a step-by-step guide are available on GitHub as well as a "cheat sheet" on wiki.
Prior to their arrival, the users are invited to follow the steps and guidelines provided here and to familiarize themselves with the software environment.

**Software functionalities:**

- All Bluesky ScanPlans and functionalities are exposed (command lines)
- Easy management of the list of samples through a spreadsheet that can be filled prior to the experiment
- Calibration procedure (distance to detector, center-of-beam, etc)
- XPD custom ScanPlans (xpdAcq) that are compact and easy-to-use for such tasks as a single image count (*ct*), a series of images over time (*tseries*) or as a function of temperature (*Tramp*)
- The analysis pipeline (xpdAn) automatically processes, saves and visualizes the data in real time:
    - Raw 2D diffraction images
    - 2D diffraction images corrected for electronic background and polarization
    - auto-masked and background-subtracted 2D images
    - integrated scattered intensity, I(Q) and I(tth)
    - the structure and reduced structure factors S(Q) and F(Q)
    - the PDF G(r) curve
- Manage and save the metadata
- Write more advanced scripts

xpdAcq has provision to integrate fully automated workflows (as described in section 5.4) and make an extensive use of metadata that capture sample provenance and keep track of experimental and theoretical data log related to each sample.
xpdAn is designed to grow into a suite of tools that take advantage of the most recent computational techniques (database mining, machine learning, pattern searching and matching, …).

# 3 - Scientific Program

XPD is designed to address the new trends in Powder Diffraction and Structural Studies:

- high penetrating power (bulk, high Z, measure through a device or cell)
- time-dependent, fast and real-time observation (transient, pathways), *i.e*. away from equilibrium and static
- *In situ*, operando & extreme environments
- high throughput (large batch of samples, combinatorial)
- extended Q-space (PDF, real space analysis to examine short-range order)
- real & complex samples, *i.e*. away from ideal crystals (defects like stacking faults, disorder, multi-phase,…)
- multiple length-scale measurements (combined scattering techniques: XRD, PDF and SAXS)

The science opportunities for XPD reside in:

1. *In situ* Synthesis & Materials by Design (application to MOFs and nanostructures, Li-ion cathode materials, high-Tc superconductors,…)
2. *In situ* and operando structure evolution (application to catalysts, cycling battery materials, Solid Oxide Ceramics,…)
3. Combinatorial & High Throughput Structure Analysis (application to nuclear materials, energy materials, engineering materials,…)

Science scope and impact (published work only) are described in Appendix 1.
The published work using XPD capabilities can be grossly divided in 8 categories (Fig. 7):

1. Chemistry: *ex situ* structure on recovered or as-prepared samples *vs*. synthesis conditions, composition, doping, etc.
2. Physics: structure and physical properties relationship (superconductors, magnetic transitions, quantum, thermoelectrics, negative thermal expansion)
3. Battery and energy storage materials. This can be sub-divided into i) structure of battery materials and relationship with electrochemical performance (68%); ii) structural transformations operando (23%); iii) *in situ* synthesis of battery materials (9%).
4. Synthesis (*in situ* structural measurements)
5. Materials processing (flash sintering and materials engineering)
6. Nuclear science
7. Instrumentation, detectors, methods
8. Other (earth science, gas and organic molecule sorption studies, catalysis)

This categorization is certainly not exact and suffers from many overlaps[4], but is meant to identify the core research activities at XPD. Also, some categories are technique- or objective-based, others are materials-based.

Battery research is seen to bring in the dominant class of materials (1/3).
The *in situ* category is "only" 13%. This does not at all reflect the amount of work that is actually invested into *in situ* measurements; instead it reveals that the "return-on-investment" of *in situ* work is delayed since several cycles of development and experiments are often needed until the set-up is finally functional and yields reliable results. Appendix 3 shows the extensive list of *in situ* capabilities, most of them requiring a substantial effort for integration into controls and software.

[4] For example, materials processing (#5) and sorption studies (#8) both are *in situ* structural measurements. Nuclear science (#6) also uses the flash sintering method (#5). Or nuclear science (#6) could also be imbedded in the ex situ category (#1). The boundary between #1 and #2 (1/3 of the XPD published work) is also "fuzzy": #1 is viewed more from a chemistry perspective (*e.g*. structure as a function of the synthesis conditions), while #2 deals with the relationship between structural features (short- and long-range) and the physical properties.

**Figure 7: Topical Distribution of Publications**

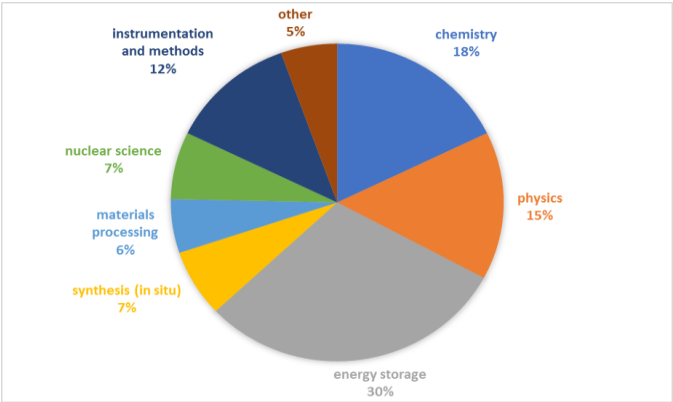


XPD has been very successful thus far in addressing a wide variety of experiments, even though a part of its instrumentation, control and software is still in its infancy or in the ramp-up phase.

# 4 - Productivity and Impact

**Figure 8: XPD Proposal Allocation (Sep. 2015 through May 2018)**

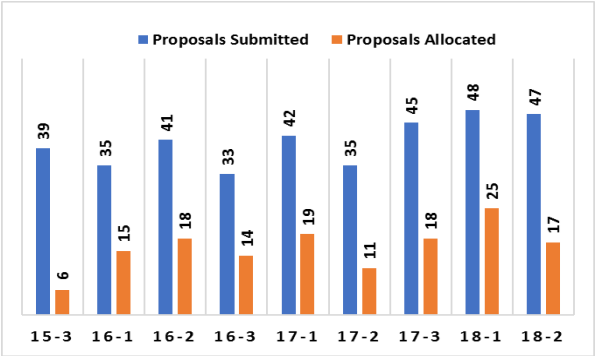


where proposals allocated include new proposals as well as 2nd- and 3rd-time beamtime requests[5]

- Subscription rate = 2.5 (# submitted proposals / # approved proposals) (2.3 over the last 3 run cycles - see Fig. 8)
- Publication rate = 1.4 (# approved proposals through end of CY17 per total # publications) (2.0 with a less conservative calculation)
- Number of users per proposal is 6±1
- 1/3 of the XPD users come from non-Eastern US and overseas (Fig. 10)

[5] GU proposal lifetime is 3 cycles

**Table 2: User Time Partition**

| | | |
|---|---|---|
| General Users | GU<br>Scoring of the scientific merit done by the High Energy Diffraction Proposal Review Panel[6] | |
| Partner Users* | PU (≤ 40% by policy[7]) | – 9% S. Billinge – BNL-University of Columbia (new agreement pending)<br>– 6% L. Ecker – BNL-NSUF<br>– D. Weidner – COMPRES – Stony Brook University (agreement pending) |
| Beamline Discretionary Time | BDT (≤ 10% by policy[7]) | |
| Proprietary Research | PR | – Pfizer. 1 shift in 2017-3<br>– SynchXray, L.C. 1 shift in 2018-1 |

*see Appendix 4

**Figure 9: Fraction of User Beam Time** (user available time* = GU+PU+BDT+PR)

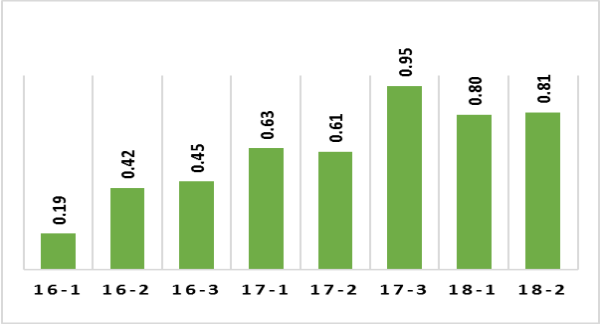


*where GU stands for General User, PU for Partner User, BDT Beamline Discretionary Time and PR Proprietary Research.

The (commissioning time/user time) ratio seems to level off over the last 3 cycles at around 20:80.

**Figure 10: Geographic origin of the XPD users[8]**

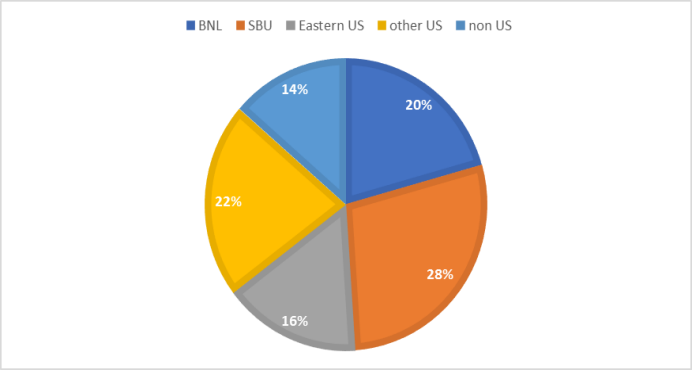


[6] https://www.bnl.gov/ps/docs/pdf/PRP-Members.pdf
[7] NSLS-II Guide to Proposal Types at https://www.bnl.gov/ps/access/proposals.php
[8] Each user who came to the floor is counted only once, regardless the number of proposals or experiments

**Table 3: Number of Users on the XPD floor through Aug. 2018**

| Cycle | Users by Cycle |
|---|---|
| 2015-3 | 43 |
| 2016-1 | 74 |
| 2016-2 | 95 |
| 2016-3 | 72 |
| 2017-1 | 99 |
| 2017-2 | 114 |
| 2017-3 | 95 |
| 2018-1 | 113 |
| 2018-2 | 126 |

| Cycle | Unique users by CY |
|---|---|
| 2015 | 52 |
| 2016 | 127 |
| 2017 | 151 |
| 2018 | 150 |

**Table 4: Number of XPD Publications**

| 2013 | 2015 | 2016 | 2017 | 2018 | **total** |
|---|---|---|---|---|---|
| 1 | 4 | 19 | 28 | 21 | **73** |

**Table 5: XPD Science Highlights**

- Terban, M., et al. (2018) "Tracking the Early Stage Growth of Metal Organic Frameworks" Nanoscale 10, 4291-4300(2018) DOI Link
- Sun, K., et al. (2017) "Multimodel Approach Gives New Insights Of Lithium-Sulfur Batteries" Sci. Rep. 7, 12976 (2017) DOI Link
- Tyson, T.A., et al. (2017) "Electron Mobility Is Key For Possible New Solar Cell Material" Scientific Reports 7, 9401(2017) DOI Link
- Simos, N., et al. (2017). "Neutron irradiation and high temperature effects on amorphous Fe-based nano-coatings on steel – A macroscopic assessment." Journal of Nuclear Materials 489: 164-179. DOI Link
- Hudry, D., et al. (2016)."Probing the Crystal Structure and Formation Mechanism of Lanthanide-Doped Upconverting Nanocrystals." Chemistry of Materials 28(23): 8752-8763. DOI Link
- Hu, E., et al. (2016)."Explore the Effects of Microstructural Defects on Voltage Fade of Li- and Mn-Rich Cathodes." Nano Letters 16(10): 5999-6007. DOI Link
- Jensen, K., et al. (2016) "Polymorphism in magic-sized $Au_{144}(SR)_{60}$ clusters." Nature Communications, (2016)7: 11859. DOI Link
- Wangoh, L.W., et al. (2016) "Correlating Lithium Hydroxyl Accumulation with Capacity Retention in $V_2O_5$ Aerogel Cathodes" ACS Appl. Mater. Interfaces, 2016, 8 (18): 11532–11538 DOI Link
- Sprouster, D.J., et al., (2016) "Structural characterization of nanoscale intermetallic precipitates in highly neutron irradiated reactor pressure vessel steels" Scripta Mat., 2016, 113:18-22 DOI Link
- Xu, J., et al. (2016) "Elucidation of the surface characteristics and electrochemistry of high-performance $LiNiO_2$" Chem. Commun., 2016, 52, 4239-4242. DOI Link
- Jensen, K., et al. (2015). "Demonstration of thin film pair distribution function analysis (tfPDF) for the study of local structure in amorphous and crystalline thin films" IUCrJ (2015) 2: 481-489. DOI Link
- Wu, L., et al. (2015) "Structural Defects of Silver Hollandite, $Ag_xMn_8O_y$ Nanorods: Dramatic Impact on Electrochemistry." ACS Nano, 2015, 9(8), 8430-8439. DOI Link

**Table 6: XPD features published in BNL Website Newsroom**

- 06/2018 - Tripling the Energy Storage of Lithium-Ion Batteries
- 05/2018 - Maxwell Terban Receives 2018 Julian David Baumert Ph.D. Thesis Award
- 05/2018 - Multi-Modal Operando X-Ray Study Yields New Insights on Lithium-Sulfur Batteries
- 12/2017- 2017's Top 10 Discoveries and Scientific Achievements at Brookhaven National Laboratory
- 10/2017 - Stony Brook Scientists Solve Fundamental Puzzle in Medical Imaging
- 08/2017 - Scientists Find New Method to Control Electronic Properties of Nanocrystals
- 05/2017 - A Nanostructured Iron-Alloy Coating Beefs Up Nuclear Steel
- 06/2016 - Discovery of Gold Nanocluster "Double" Hints at Other Shape-Changing Particles
- 03/2016 - 'First Light' Experiments at NSLS-II Study Radiation's Effect on Reactor Pressure Vessels
- 08/2015 - Investigating Metal-Organic Frameworks as Clean-Up Agents for Nuclear Waste
- 08/2015 - Brookhaven Lab Study Explores Nanoscale Structure of Thin Films
- 03/2015 - First Scientific Publication from Data Collected at NSLS-II
- 01/2015 - Compact Batteries Enhanced By Spontaneous Silver Matrix Formations
- 11/2014 - X-Ray Powder Diffraction Beamline at NSLS-II Takes First Beam and First Data
- 04/2014 - Disorder on the Nanoscale May Be Responsible for Solar-cell Efficiency
- 08/2013 - Bright Light, Big Mirror: Precision X-ray Focusing at NSLS-II

A few science highlights are shown in Appendix 1.

# 5 - Vision for Next Five Years

## *5.1 - Battery and Energy Storage*

Given the track-record of the XPD beamline in battery and energy storage, we expect this research area will continue to grow as XPD is expanding its *in situ* and operando capabilities. XPD is now equipped with a cycler and has the hardware and software to probe several batteries in a series of repeated successive measurements while the batteries are being charged and discharged. Such experiments can be done in endstation 1 but longer lead time measurements can be accommodated in endstation 2 (section 5.6). The tomography set-up and the production of a small beam pave the way for mapping heterogeneities in battery electrodes.

Combined characterization using synchrotron X-ray and transmission electron microscopy techniques offers new opportunities for in-depth studies of ion transport, electrochemical reactions, and phase transformations over wide length and time scales[9,10]. X-ray diffraction, associated with XAS and TEM, is applied to exploring the structural origin of the overcharge induced thermal instability of two cathode materials[11,12] and lately applied to resolving the local structural ordering and defects (*i.e.* oxygen deficiency) for direct correlation with the electrode performance [xpd-2].

[9] Goodenough, John B., H. D. Abruna, and M. V. Buchanan. "Basic research needs for electrical energy storage." Report of the basic energy sciences workshop for electrical energy storage. Vol. 186. 2007.

[10] Wang, Howard, and Feng Wang. "In situ, operando measurements of rechargeable batteries." Current Opinion in Chemical Engineering 13 (2016): 170-178.

[11] Wu, Lijun, et al. "Structural origin of overcharge-induced thermal instability of Ni-containing layered-cathodes for high-energy-density lithium batteries." Chemistry of Materials 23.17 (2011): 3953-3960

[12] Nam, Kyung-Wan, et al. "Combining In Situ Synchrotron X-Ray Diffraction and Absorption Techniques with Transmission Electron Microscopy to Study the Origin of Thermal Instability in Overcharged Cathode Materials for Lithium-Ion Batteries." Advanced Functional Materials 23.8 (2013): 1047-1063.

## *5.2 – Advanced Manufacturing*

The development of advanced manufacturing approaches is a shared DOE/DOC/DOD/NSF agency goal. In this field, XPD can contribute: i) instrumentation for high-throughput ex-situ studies and *in situ* growth and processing studies and operando studies that link structural, chemical, electronic properties to material or device performance; ii) high-performance computing for real-time analysis, efficient parameter space exploration, and optimal extraction of information from complex data sets

## *5.3 – In Situ Synthesis*

Amongst the urgent challenges for materials scientists in the 21st century is the discovery of transformational materials (TM) for energy production, storage and for mitigating the environmental consequences of energy usage. Development of TMs is based not only on the knowledge of their static structure, but more appropriately on an understanding of how the structure changes during operation under real working conditions.

Theory and experiment can be integrated in a closed loop in exploratory syntheses, where theory can identify theoretical desired materials that are thermodynamically stable, and *in situ* XRD synthesis could then be used to pinpoint the feasible synthetic routes. With this new approach in mind, XPD seeks to develop the tools that will enable the discovery of novel functional materials, as well as optimize their synthesis and processing.

*In situ* synthesis will be a recurrent theme. One recently started project[13] (coll. J. Owen - Univ. of Columbia) consists in a detailed study of the formation of colloidal semiconductor nanocrystals using XPD's time-resolved techniques. The plan is to build and deploy a flow cell at the XPD beamline and to couple this with high throughput data acquisition methods. A library[14] of sulfur and selenium precursors and modeling (Coll. UC Santa Barbara) will be used to unravel the fundamental mechanism of PbS, PbSe, CdS, and ZnS nanocrystal nucleation and growth. Assisted by Monte Carlo algorithms, high-throughput and real-time SAXS and WAXS will enable to extract the reaction yield, the nanocrystal size and size distribution in the flowing solution. PDF will be used to extract the size of the crystalline domains during nucleation, as well as the lattice parameters, stacking faults, and strain as the nanocrystals grow.

## *5.4 – Enhanced Capabilities*

Moving forward, XPD aims at establishing its competitive edge by implementing/strengthening these following capabilities:

1. **Automation**. It will soon be possible to load all samples in a magazine, then synchronize and run the robot, the photon shutter and attenuation filters, trigger both the near-field AND the far-field detectors, while using either the low- or high-temperature device (100K – 1,000°C). The software will also determine upfront the optimum acquisition conditions for each sample (*i.e*. best statistics with no saturation). Machine learning technique may even help streamline the workflow. This high-throughput capability will be unique in the US.
   Automation is particularly relevant for hazardous materials and radioactive materials[15].

[13] Proposal for facility-supported Research, Development and Improvement Project – approved 2018.

[14] J. Owen et al. Science, 2015; JACS, 2017

[15] Funding Opportunity Announcement (DE-FOA-0000799 by Department of Energy, Idaho Operations Office) titled: 'Automated Synchrotron X-ray Diffraction of Irradiated Reactor Pressure Vessel Steels' 2013-2016. PI: L. Ecker – BNL.

This also causes XPD to transition from experiments to measurements (section 5.4). Current thinking is to automate XPD in the future for ~1/3 (TBD) of the user time. This will free up time for more difficult tasks that need the presence of users and support/expertise of beamline staff.

2. **High resolution**[1]: the 'fast and dirty' mode of XPD applies to a very large majority of *in situ* or operando diffraction experiments. However, XPD has provision (since its inception) for achieving a better angle resolution using post-sample analyzer crystal optics and angle-scanned detectors using a high-energy photon beam (section 5.7.4.1). We believe XPD can thrive between the 'fast and dirty' mode and the 'slow and clean' mode. Higher resolution will help identify complex and transient phases in solid state synthesis. It is proposed to combine the Debye-Scherrer configuration (where resolution is driven by the detector slit opening) and the analyzer configuration in one single scan.

3. **Sample environment** (incl. extreme conditions): we shall continue to extend our pool of sample environments and *in situ* synthesis and materials processing capabilities. Most of this development will be coordinated in collaboration with the user community. XPD will leverage its recently installed gas handling system (with provision for toxic gases), to enable *in situ* / operando experiments involving chemical reactions, catalysis and particle nucleation/growth using gas-solid and colloidal synthesis methods.

   In the near future, a part of the XPD *in situ* effort will be directed toward structural characterization of molten salts. The overall importance of molten salts to enable breakthroughs in next-generation reactors is highlighted in the 2018 DOE Basic Energy Sciences (BES) Basic Research Needs for Future Nuclear Energy workshop report (BRN-FNE), where the first Priority Research Direction is, "Enable design of revolutionary molten salt coolants and liquid fuels". Fundamental issues concerning molten salts and their interactions with solutes and materials are central to enabling advanced MSR designs and stable reactor operation over wide ranges of temperature and radiation flux. XPD is a partner of the center for Molten Salts in Extreme Environments (MSEE)[16] with a goal to develop a fundamental and predictive understanding of molten salt bulk and interfacial structural features.

4. **Diffraction tomography and imaging**: focusing optics (section 5.7.2) and spiderweb slits (section 5.7.1) will contribute to using the XPD beam with higher spatial resolution for mapping and imaging, combining XRD and PDF.

   An important application of non-invasive imaging is the full high-resolution, high-sensitivity, structural, mineralogical, morphological and chemical *in situ* characterization of returned samples from Mars without breaking containment (samples are sealed in 0.50mm thick Ti-alloy tubes). The high-energy X-ray CT-XRD of XPD is believed to be an excellent match. XPD preliminary experiments are shown in Figs. 11 and 12.

[16] U.S. Department of Energy Office of Basic Energy Sciences For: Energy Frontier Research Centers (EFRC) DE-FOA-0001810 titled: 'Molten Salts in Extreme Environments'. PI: J. Wishart - BNL. 2018-2023.

**Figure 11:** X-ray diffractograms of the banded iron formation sample between two Ti6Al4V alloy plates of 0.52mm thickness, without (A) and with (B) the two plates in the path of the X-ray beam. The analysis of the **d**iffractograms are in both cases the same, showing identical fractions of quartz and goethite in the sample. This shows that the influence of the two Ti6Al4V plates is negligible for such measurements.

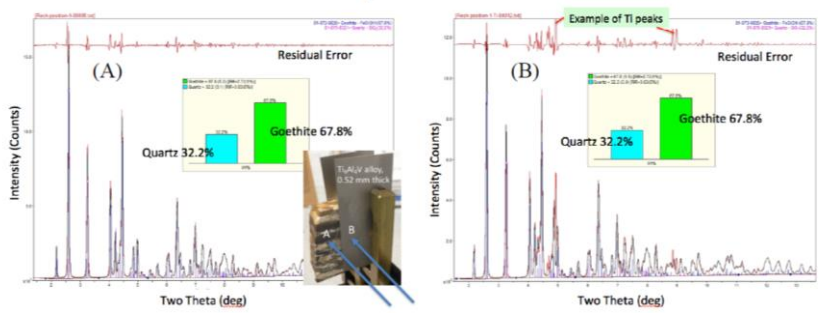


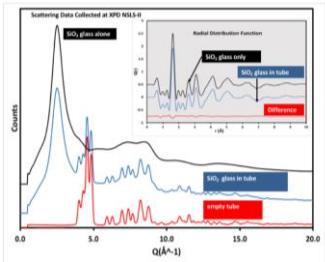


**Figure 12:** PDF proof-of-concept measurement of Si glass in a Ti-alloy tube. PDF signals for Si glass only, Si glass contained in Ti-alloy tube and tube alone. Inset shows that by subtracting the contribution from the tube, the PDF signal from the Si glass can be extracted with high fidelity (*i.e.*, two radial distributions curves are essentially identical).

5. **Software**: XPD throughput and productivity can be (and will be) augmented by the advent of new theory-and computer-assisted predictive tools: i) automated database queries and search-and-match routines to identify and compare data coming off the detector with experimental and/or calculated data. Tests have started with the open-web based Materials Project[17]; ii) self-similarity or Principal-Component-Analysis (PCA[18]) algorithms to detect on the fly changes in a flow of diffraction patterns over time that can reveal a genuine structural effect like a phase transition (or an instrument artefact like a beam energy shift); iii) machine-learning techniques taking advantage of the large datasets that XPD generates. See application in section 5.5.

## *5.5 – From High-Throughput Science to Materials Design*

To be useful, a material must be made, and its synthesis must then be optimized, regardless of how it was conceived or serendipitously discovered. Control over synthesis pathways and products is a critical requirement for materials design. Therefore, the design of the next generation of materials requires a means to detect the changes and intermediates occurring along a reaction pathway. *In situ* tools should allow to track the physical and chemical changes occurring along a set of tentative pathways, provide the critical data required for i) the development of the atomic scale modeling of synthesis, and ii) to rationally steer the reaction through new pathways and toward optimized

[17] https://materialsproject.org/
[18] B. K. Alsberg, V. R. Jensen and K. J. Borve, J. Comput. Chem., 1996, 17, 1197.

materials, and generates the raw minable data for machine learning of what manipulations lead to which optimized products.

A first attempt at this 'material by design' approach is nicely illustrated in [xpd-3] (appendix 1). Another example is [xpd-4] (appendix 1), where energy barriers are calculated to predict reaction path and explain the *in situ* XRD measurements.

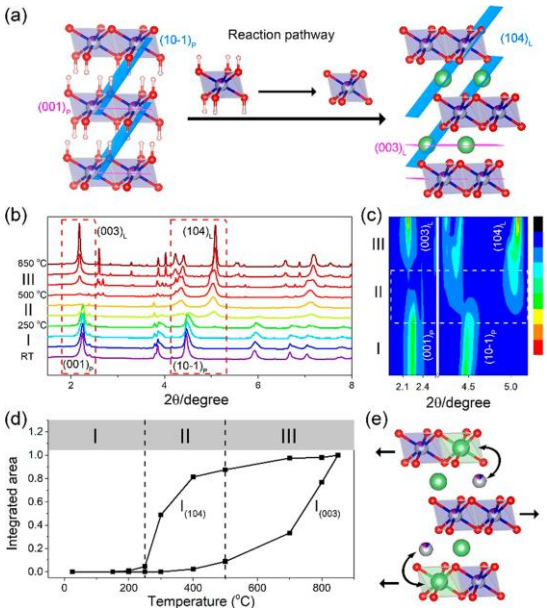


**Figure 13** [xpd-4]: Structural transformation during solid-state synthesis of the layered LiNi0.73Mn0.13Co0.10O2 (NMC771310) from the hydroxide precursor Ni0.73Mn0.13Co0.10(OH)2. (a) Schematic of the transformation from layered hydroxide precursors (P-3m1) to layered oxides (R-3m), and the corresponding change in the BBUs, from initial TM(OH)6 to the TMO6 octahedra. (b) Temperature-resolved in situ synchrotron XRD patterns, showing three sequential stages during the entire synthesis process: I (below 250 °C), II (250–500 °C), and III (above 500 °C). (c) Contour plot of selected regions in XRD patterns (marked with red dashed rectangles). (d) Evolution of integrated intensities of (003) and (104) peaks (denoted as I(003) and I(104), being normalized to their corresponding values at 850 °C), which reflect the behaviors of cationic disordering/ordering (by I(003)) and Li insertion (by I(104)) as the temperature increases. (e) Schematic of atomic rearrangement, interlayer gliding, and Li/Ni mixing (illustrated by arrows) in the intermediate (Ni0.77Mn0.13Co0.10(OH1−xLiy)2) during Stage II.

Orders of magnitude more data will be generated when synthesis pathways (and not just products) are studied, and new tools for a data-driven approach to synthesis will need to be developed. We think that the XPD hardware and software infrastructures are ideal to address this challenge and help accelerate mapping of reaction space using and enhancing its high-throughput *in situ* diagnostics and data analytics.

The EFRC GENESIS[19] provides the framework, expertise, collaborations and resources to establish some of the tools and methods needed to understand the non-equilibrium pathways that govern synthesis by elucidating their relationship to synthesis variables.

Data analytic approaches will be developed that both make predictions for new recipes based on training datasets, but also guide the experiments so that predictions are made about process input parameters for future experiments, rather than the experimental searches being done in a combinatorial way. This approach represents a true paradigm shift away from isolated studies of single reaction products to computationally-enabled comprehensive studies of thousands of pathways.

The *in situ* data collection will be automated, including data reduction and model fitting, and results streamed to a database of experimental results, where complete metadata of the process parameters will be stored along with the resulting structural information obtained.

Machine learning (ML) will be applied to the training data to search for relevant features and to seek correlations between input parameters and outcomes. This approach will be used both to guide

[19] Funding Opportunity Announcement DE-FOA-0001810 DOE/Office of Science Program Office: Basic Energy Sciences. '*GENESIS: A Next Generation Synthesis Center*'. PI: J. Parise – Stony Brook. 2018-2023.

future experiments and to make predictions about novel synthetic pathways for desirable material structures (or properties).

## *5.6 – Long Duration Experiments*

XPD endstation 2 is also intended to be used for those measurements that require long lead-time preparation, *e.g.*, a gas rig or a spectrometer. Endstation 2 is an opportunity for long duration experiments: the beam can be sent intermittently into the downstream hutch to enable short and repetitive measurements at regular intervals over a long period of time *i.e.*, corrosion studies, slow growth processes, charging and discharging of batteries, degradation of cathodes and anodes in fuel cell research, environmental effects on solar cell materials. This development has not started but has the potential for a high user demand. The only equivalent of this is at the I11 – Long Duration Experiment beamline[20] at the Diamond Light Source (UK).

Work is in progress to permit a rapid change-over of the beam back-and-forth between endstations 1 and 2.

## *5.7 - Instrumental Development*

### 5.7.1 – Enhanced Space Resolution

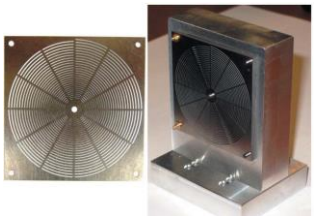

This project was developed as a Laboratory Directed R&D (LDRD) – '*Conical/spiral slit for 3D spatially resolved X-ray diffraction'*. PIs: Ray Conley and Nathalie Bouet (BNL) and produced a patent and a publication.
This so-called spiderwell slit system is being tested at XPD, in particular with the large volume press (section 5.7.3).

U.S. Patent Office - December 12, 2017 (Serial Number 15/839,413) - Title: "X-Ray Filter For X-Ray Powder Diffraction" by: Sinsheimer, John; Bouet, Nathalie; Ghose, Sanjit; et al. J. of Synchrotron Radiation 23 (2016) 1296-1304 - DOI Link.

xpd-5 'Fabrication and testing of a newly designed slit system for depth-resolved X-ray diffraction measurements' by: Sinsheimer, John; Bouet, Nathalie; Ghose, Sanjit; et al. J. of Synchrotron Radiation 23 (2016) 1296-1304

### 5.7.2 - Diffraction-Tomography

The XRD-CT equipment (Fig. 14) is designed to provide morphological and structural information for engineering scale samples. It will facilitate a science-based approach for a wide variety of materials (metals, ceramics, composites, concretes and nanocrystalline materials) with limited, to no, sample preparation. It will be applied primarily in Nuclear Science to designing new materials for advanced reactors, understanding materials degradation mechanisms, supplying data for materials qualification

[20] C. A. Murray, J. Potter, S. J. Day, A. R. Baker, S. P. Thompson, J. Kelly, C. G. Morris, S. Yang and C. C. Tang "New synchrotron powder diffraction facility for long-duration experiments". J. Appl. Cryst. (2017) 50, 172-183

for licensing, and evaluating manufacturing processes. Unlike traditional X-ray computed tomography that is based on X-ray absorption, XRD-CT is meant to simultaneously supply crystallographic structural information with spatial resolution set by the beam size (~20µm).
The diffraction-tomography hardware in endstation 2 is supported by DOE-NE[21].

**Figure 14: CT-XRD assembly in endstation 2**

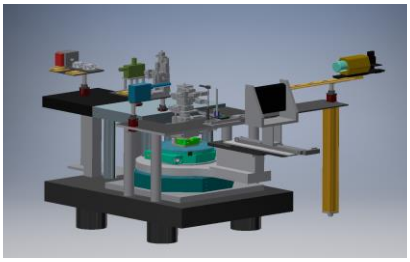

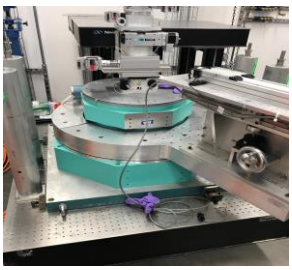

Equipment comprises a 2-circle Huber diffractometer (repurposed from NSLS), optical breadboard tables, stack of rotation-translation stages for sample (Huber), a CMOS flat panel detector (®Varex Imaging), beamstop and support and alignment kit, beam slits and aperture pinhole system (JJXray), kinoform lenses (in-house, K. Evans-Lutterodt) and hexapod support, a full field x-ray imaging system, capillary mirror and alignment system (®Sigray) capable of focusing the 67keV beam to 30µm × 20µm

## 5.7.3 – High Pressure

XPD endstation 2 hosts a multi-anvil system that consists of a 1,000 ton press driving different types of guideblocks (DT-25, DDIA, T-10), a flat-plate detector and a beam diagnostic system (YAG crystal + camera and a photodiode) that rest on a table.
This high pressure and high temperature experimental deformation/rheological technique and the *in situ* ultrasonic interferometer are maintained and operated by the Mineral Physics Institute (see User Partnership in appendix 4) and more details can be found here. The beam typically is 100-250µm for diffraction (much larger fattens the rings) and 3mm by 3mm for imaging.

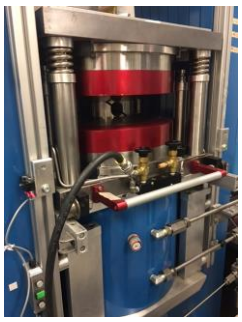

The DT-25 deformation module is the first of its kind in the world, capable of performing deformation studies on Earth, ceramic, novel, and functional materials at higher pressures than anywhere else. This apparatus has allowed for the first data to be collected on the rheological properties of $CaSiO_3$, which is an important phase found deep within the Earth's mantle.

This equipment is primarily designed for Earth Science (P-V-T Equation of State, phase and melting relations *in situ* at lower mantle conditions, rheological properties, anelasticity, plasticity,…). Materials Science (phase transformations, compressibility, thermoelastic properties, high-pressure synthesis,…) will also be using this equipment.

[21] Funding Opportunity Announcement (DE-FOA-0001130) for General Scientific Infrastructure, DOE, Idaho Operations Office 2015-2018 '*X-ray Synchrotron Diffraction Tomography for Materials for Nuclear Energy Systems*'. PI: L. Ecker – BNL.

## 5.7.4 – Detectors

### 5.7.4.1 – Detector high-resolution Multi-Analyzer System (MAD)

XPD will offer the option of a high-resolution configuration by trading a unique system composed of 8 channels fitted with analyzer Laue crystals for the 2D detectors. This concept is new and will use two distinct detector units developed in house, that are angle-scanned simultaneously and collect the sample-diffracted signal with and without the analyzer crystals. One unit is an array of photomultiplier tubes associated with GYSO scintillator crystals (Fig. 16). The second unit is an array of 8 × 8 CdZnTe chips (Fig. 17).

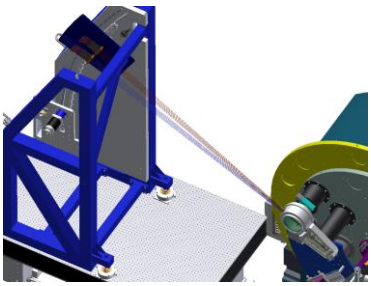

**Figure 15:** Model shows the analyzer crystal box mounted on the diffractometer and the 2 sets of detectors (left).

**Figure 16: XPD PMT/scintillator detector**

Specifications:

- 8 ®Hamamatsu Photo-Multiplier Tubes (PMT) is 10.5mm diameter (8mm Ø active area).
- Each scintillator is a GYSO:Ce crystal 10mm Ø x 3mm.

Integration and testing to be done.

**Figure 17: XPD CZT-based multi-strip detector**

Specifications:

- 16 strips per sensor (125m)
- 8 sensors
- 128 channels
- 2 BNL-designed 64-channel readout chips
- 40nsec deadtime
- 128GB SSD
- 10(15) kHz data reading (28Mb/s 16bits/sensor and 16 sensors per channel

Integration and testing to be done.

## 5.7.4.2 - Germanium microstrip detector

The detector combines the low-noise integrated circuits developed at BNL[22] with commercially available segmented germanium detectors with excellent pixel-pixel isolation made by ®Semikon.

**Figure 18: NSLS-II Ge strip detector**

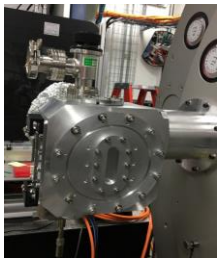

Specifications of one module are:

- 125µm pixel pitch
- 385 pixels
- 48mm high

Options for the future are:

- customize size and shape (strip of 5 interleaved modules)
- change pixel size to 150µm
- extend to 640 strips of 125 µm (larger angle coverage)

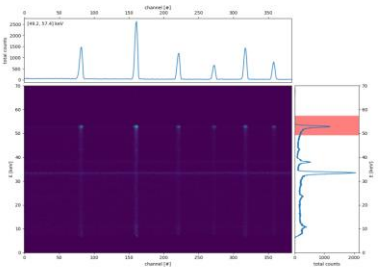

Benchmarking at XPD:
intensity vs. pixel position and energy of a LaB6 NIST standard.

right-hand panel shows energy spectrum: elastic peak, Ge escape peak, La Kß and Kα fluorescence peaks.

Diffraction pattern (top panel) is generated by selecting an energy ROI (orange area)

The unique features of this detector [xpd-6] are its energy resolution (combined with the pixel-angle resolution) and the time stamping and time slicing (10msec) capabilities for hyperspectral (2θ, time, energy) imaging. The GeRM detector game-changing capabilities are:

- high detection efficiency (compared with the more established Si technology)
- angle resolution driven by its small pixel size
- arrangement of the modules in an array that permits to let the main beam through for example (small angle scattering)
- time slicing: recompose the data to determine diffracted intensity as a function of angle at any particular time
- angle slicing: recompose the data to determine diffracted intensity as a function of time at any particular 2θ angle.
- energy discrimination (eliminates inelastic scattering)

xpd-6 A Rumaiz, A Kuczewski, J Mead, E Vernon, D Pinelli, E Dooryhee, S Ghose, T Caswell, D Siddons, et al, Multi-element Germanium Detectors for Synchrotron Applications, *J. Instrum.*, **13**(C04030) (2018).

[22] A. K. Rumaiz, et al, IEEE NSS 2013

#### 5.7.4.3 - CdTe Photon-Counting Pixel detector

XPD has been operating with a-Si (CsI scintillators) flat panel detectors (®Perkin-Elmer). These detectors probably do a fair job, but have severe limitations:

- "small" dynamic range (12 bits)
- high background
- read-out noise
- signal remanence (ghost image after exposure)
- low frame rate (10 Hz)

In the high-energy x-ray range, CdTe-based pixel-array photon counting detectors (like the Pilatus camera ®Dectris) is the new state-of-the art and would have a significant impact on the data quality and reliability at XPD.

### 5.7.5 - New Methods

In addition to understanding static or steady-state atomic structures of materials, it is important to understand how they evolve during operation under real working conditions, such as an electrode material in a charging and discharging battery or a catalyst material functioning during the abatement of exhaust gases in vehicles. The Modulation Enhanced Diffraction (MED) method has been implemented as a new characterization tool to recover information, which is otherwise buried in the larger signal emanating from the predominantly passive part of the structure. The aim of this project was to expand the *in situ* and operando time-dependent diffraction capabilities at the XPD beamline.

MED is a well-established technique in spectroscopy, but very new in powder diffraction. This project[23], which developed procedures and algorithms to implement MED, stems from a collaboration between Brookhaven, Argonne and Stony Brook University. Structural selectivity is enhanced in MED by cycling an external parameter, such as the reactant composition, temperature, pressure, or electrical field during the course of the diffraction measurement. For example, MED can be used to track the relative proportions of copper (Cu) and copper oxide ($Cu_xO$) supported on ceria (CeO2) in several catalysts. Procedures to implement MED were developed and benchmarked by studying the oxidation and reduction of a mixture of Cu and $Cu_xO$. The measurements were conducted by periodically pulsing $H_2$/CO gases over the catalyst. When the catalyst goes from inert to active, MED can detect the small structural changes that allow for the catalyst to selectively remove CO from a mixture of CO and $H_2$, prior to input to fuel cells. MED can uncover subtle changes normally undetected by conventional diffraction methods. Also importantly, MED can be executed over the timescale of interest for most functional materials, which ranges from seconds to minutes or even hours.

This project was selected as a highlight for inclusion in the Office of Science 2016 LDRD Brochure, for its relevance to the DOE Strategic Plan.

[23] LDRD #13-031'*Modulation Enhanced Diffraction: a new tool for powder diffraction and total scattering studies*'. PI: Eric Dooryhee. 2013-2016.

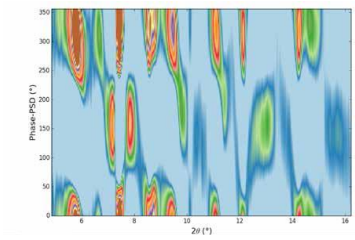


**Figure 19**: Oxidation-reduction of Cu60Ce40 in Oxidation-reduction of $Cu_{60}Ce_{40}$ in pulsing $H_2/O_2$ gases at 250°C in a constant stream of $CO/O_2$ mixture. The demodulated powder patterns as a function of phase angle are shown, where Cu, CuO, and $Cu_2O$ phases can be distinctly identified.

Publication output is:

Caliandro R, Guccione P, Nico G, Tutuncu G, Hanson JC . Tailored multivariate analysis for modulated enhanced diffraction. JOURNAL OF APPLIED CRYSTALLOGRAPHY 48 (2015) 1679-1691 (2016)

Caliandro, R., et al., "Static and Dynamical Structural Investigations of Metal-Oxide Nanocrystals by Powder X-Ray Diffraction: Colloidal Tungsten Oxide as a Case Study." Chem. Phys. Chem. 17(5), 699–709 (2016).

# 6- Beamline Self-Assessment

## *6.1- Reliability of XPD Operations*

1. **heat load management**: extensive FEA simulations, careful design and manufacturing of the fixed aperture mask and filters were critical to accommodate the high incident total power (kW) and peak power density ($kW/mm^2$) (Fig. 1). All filters are functioning, and the monochromator first crystal proves to be very stable (no thermal drift). Fig. 20 shows that other beamlines with similar heat load levels have had issues.

**Figure 20:** Failure of SiC filters (left) and a Laue crystal (right) at a high power wiggler beamline

2. **The Double Crystal Monochromator** (DLM): The XPD monochromator design is based on the concept proposed by Z. Zhong[24]. The crystal is mounted on a bending mechanism which is designed to vary the sagittal as well as the meridional bending with energy. The sagittal bending of the Laue crystal provides focusing of the incident fan in the horizontal plane. The anticlastic bending in the meridional plane is used for improved energy resolution. The meridional radius is adjustable and related to the sagittal radius.
   The DLM is the first optical element and cryogenic cooling of the crystal is required in order to minimize crystal thermal distortion and therefore maintain beam quality. The control of both the sagittal and the meridional bending radii under high thermal load is key to the performance of the beamline.

[24] Z. Zhong et al. "Sagittal focusing of high-energy synchrotron X-rays with asymmetric Laue crystals. II. Experimental studies", Journal of Applied Crystallography 34 (2001) 646-653.

To mitigate risks, a prototype of the DLM first-crystal assembly was first produced and tested at the I12 beamline at the Diamond Light Source. The specification, procurement, design, manufacturing and commissioning of the DLM have been a very involved process.

Eventually DLM is performing extremely well and operations of the DLM has proved to be very reliable. Changing energy and adjusting the bending of the first crystal and matching the second crystal to the first crystal remain a delicate and expert process and are far from being automated. For this reason, we minimize the number of energy changes during a run cycle and we tend to drive the DLM to known energy settings (52 and 67keV). Proposals requesting other energy settings or fine energy scanning/tuning are extremely rare.

## *6.2 - Science Focus*

The science coverage and the user community at XPD are both broad and diverse. This is a strength (high productivity; high competitiveness; many science and technical opportunities; high versatility) and a weakness (high oversubscription rate; dilution of the science focus; high work load; loss of visibility in specific areas). Past the 3 first years of operations, the science demands and the PIs are identified and XPD is on a better footing for defining and enforcing its mission (sections 3 and 5). We might try to turn this diffraction Swiss-army knife into a more specialized facility, but the inherent design of XPD, its variety of set-ups and sample environments and the pressing demand (over-subscription rate is 2.5; temporary shut-down of the powder diffraction beamline during the upgrade of the APS) from different user communities might defeat this effort. The landscape will change in the next 3 years with the PDF beamline going into production and absorbing a good part of the PDF program.

XPD is not currently configured for high-resolution diffraction and will never directly compete with beamlines like APS 11-BM, ESRF ID22 or DLS I-11. XPD is very good at tracking a transition over temperature, *i.e*. identify a new intermediate phase and measure the lattice parameters (XRD) and characterize the lower-symmetry local distortions (PDF). Crystal long-range structure solving is attempted in very rare cases at XPD for high-symmetry or sub-µm/disordered polycrystals like this organic polymorph in [xpd-7].

## *6.3 – Training*

In a sizable number of projects, excellent usable data are collected but the users are unfamiliar with the technique and/or untrained in reducing and analyzing the data. The problem becomes acute when one deals with very large datasets. Regarding the PDF technique, few groups have full expertise in the data collection strategy and adequate knowledge in the data treatment, software tools and interpretation. A mitigation is to train the users: see our first PDF workshop in 2018[25].

[25] NSLS-II Pair Distribution Function School 2018 - https://www.bnl.gov/pdfschool2018/

# Appendix 1 - User Science Program

Science cases are discussed here following the break-down of Fig. 7.
Citations in the form of [xpd-n] are work that used the NSLS-II XPD beamline in the past 3 years. This is all published work; the most recent citations may be on line, have a DOI number but journal volume and pages information is missing.
Beamline staff research essentially consists in collaborative research. This research is identified below in highlighted citations.

A few science highlights are tagged with

## *1. Chemistry (ex situ structure)*

'Structure' is understood in a very broad sense here, where a "line" is no longer drawn between short-range (PDF) and long-range (XRD) ordering.

**Magnetic 1D materials**: owing to their potential use in spintronic devices, data storage media, and magnetic resonance imaging (MRI) contrast agents[26], XPD is used to decipher the structure of cobalt-substituted pyroxene-type nanowires ($NaFeSi_2O_6$) by varying the synthesis conditions [xpd-8].

**Graphene and other 2D Materials**: 2D transition metal carbides (MXenes) consist of 2 to 4 layers of a transition metal (M) interleaved with carbon layers (X). Recently, a new subfamily of ordered layered MXenes was discovered, in which one or two layers of a transition metal (*e.g.*, Ti) are sandwiched between the layers of another layer (*e.g.*, Mo) in a 2D carbide structure. The first structural quantitative analysis of these novel materials is carried out, where PDF can determine the structure and positions of the M atoms in $Mo_2TiC_2T_x$ and $Mo_2Ti_2C_3T_x$ [xpd-9].
While more than 20 carbide MXenes have already been synthesized[27], $Ti_4N_3$ and $Ti_2N$ are the only nitride MXenes reported so far. This study shows how gas treatment synthesis such as ammoniation can transform carbide MXenes into 2D nitrides with higher electrical conductivities and metallic behavior [xpd-10].

**Functionalized Coordination Polymers**: GdIII-containing chelates stand out for their excellent properties as contrast agents (CA) and their safe use for Magnetic Resonance Imaging (MRI), in comparison to the toxic, free GdIII ions[28]. For the first time the incorporation of a GdIII macrocyclic chelate in the structure of a nanoscale coordination polymer is shown and the structure characterized by PDF [xpd-11]. This nano-structuration of the CA is envisioned as a possible mitigation for the low sensitivity, lack of selectivity and low retention of this class of MRI CA.

[26] M. Ravichandran, G. Oza, S. Velumani, J. T. Ramirez, F. Garcia-Sierra, et al., RSC Adv., 2015, 5, 17223–17227
[27] M. Naguib, M. Kurtoglu, V. Presser, J. Lu, J. Niu, M. Heon, L. Hultman, Y. Gogotsi et al., Adv. Mater., 2011, 23, 4248.
[28] A. S. Merbach, L. Helm, Ê. Tûth, The Chemistry of Contrast Agents in Medical Magnetic Resonance Imaging, Wiley, 2013.

**Photo-materials**: Lead halide perovskites such as methylammonium lead triiodide ($CH_3NH_3PbI_3$) have outstanding optical and electronic properties for photovoltaic applications[29]. Local symmetry breaking is shown that is otherwise unobservable by Bragg diffraction [xpd-12].

The interaction between cyclodextrins and perovskite precursors, methylammonium iodide and PbI2, leads to the formation of a supramolecular organic–inorganic hybrid framework importantly modifying the solution chemistry and the final film properties [xpd-13]. Generation of paramagnetic Pb3+ defects in $CH_3NH_3PbI_3$ perovskite thin film, synthesized in ambient conditions, is observed under dense optical illumination [xpd-14]. This is induced by the presence of Pb−O defects in the perovskite structure that may trap photogenerated holes.

Highly luminescent colloidal nanocrystals (NCs) of $CsPbX_3$ perovskites (X = Cl, Br, I) are investigated by X-ray total scattering techniques and the Debye scattering equation (DSE). The local structure of these NCs exhibits orthorhombic tilting of $PbX_6$ octahedra within locally ordered subdomains. This accounts for the variability of these perovskites NCs with the type of halide or temperature, defeating the classical vision of the average crystal structure [xpd-15].

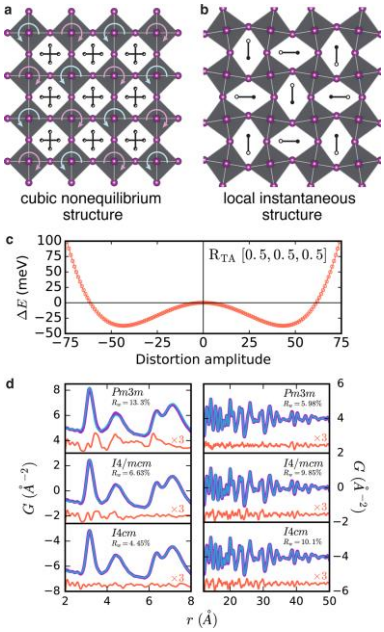


**Figure 21** [xpd-12]: Local symmetry breaking in CH3NH3PbI3 at 350K. (a,b) Distortions from cubic symmetry generate anisotropic cavities and couple to motion of the CH3NH3 + ion, which we represent as off-centered and oriented along the long axis of the cavity. (c) DFT-based lattice dynamic calculations show that the energy minimum at the R point at 350 K is displaced in a double-well potential that causes local symmetry breaking. (d) Comparison of the experimental PDF (purple) to cubic (Pm3M), centrosymmetric (I4/mcm), and noncentrosymmetric (I4cm) tetragonal models (blue) shows a superior fit for the low-symmetry models at low r (2−8 Å). However, the models perform oppositely at high r with the high-symmetry cubic structure giving the best agreement to the data in the 12−50 Å region. The residuals (orange) are scaled ×3 for clarity.

**Electrocatalysts**: 3d-transition metal (*e.g*. cobalt) oxides are among the best candidates for Oxygen Evolution Reaction (OER), a key half-reaction of water splitting[30]. However, tailoring their microstructure to enhance the performance and making them comparable to their noble-metal counterparts remain a challenge [xpd-16].

**Colloidal Nanomaterials**: Magic-sized clusters (MSCs) are clusters with elevated thermodynamic stability[31], that lie just between small molecules and quantum-confined nanostructures. The conversion of InP MSC to $Cd_3P_2$ MSC through cation exchange and the evolution of the physical and

[29] S.D. Stranks et al. Metal-halide perovskites for photovoltaic and light-emitting devices. Nat. Nanotechnol. 2015, 10, 391.
[30] Y. P. Zhu, T. Y. Ma, M. Jaroniec, S. Z. Qiao, *Angew. Chem., Int. Ed.* 2017, *56*, 1324.
[31] Friedfeld, M. R.; Stein, J. L.; Cossairt, B. M. Main-Group- Semiconductor Cluster Molecules as Synthetic Intermediates to Nanostructures. Inorg. Chem. 2017, 56, 8689–8697.

electronic structure of the clusters during transformation are described using a combination of spectroscopic and structural characterization tools [xpd-17].

**Hybrid Layered Structures**: hybrid phosphonate/phosphate compounds of formula $M(O_3PC_6H_4PO_3)_{1-(x/2)}(O_3POA)_x \cdot nH_2O$, where M = Zr and A = H or Na consist of layers of zirconium phosphate. They display no long-range order and are resistant to crystallization. These materials are of interest for their high selectivity for 3+ lanthanide ions. To investigate the mechanism of the selectivity, difference PDF analysis is used to extract the local structural environment of Tb3+ ions loaded into the framework [xpd-18].

**Perovskites**: perovskites form a particularly interesting class of materials because even slight modifications of the crystal structure can lead to dramatic changes in physical properties (superconductivity, ferroelectricity, and ferromagnetism). Pressure (up to ∼20 GPa) dependent structural measurements on monodispersed nanoscale SrTiO3 samples with average diameters of 10 to ∼80 nm are conducted to enhance the understanding of the structural phase diagram of nanoscale $SrTiO_3$ [xpd-19].


xpd-7 M Tan, A Shtukenberg, S Zhu, W Xu, E Dooryhee, S Nichols, M Ward, B Kahr, Q Zhu, ROY Revisited, Again: The Eighth Solved Structure, *Faraday Discuss*, **208** (2018) 203633

xpd-8 C Lewis, D Moronta, M Terban, L Wang, S Yue, C Zhang, Q Li, A Corrao, S Billinge, S Wong, Synthesis, Characterization, and Growth Mechanism of Motifs of Ultrathin Cobalt-substituted NaFeSi2O6 Nanowires, *Cryst. Eng. Comm*, **20**, 223-236 (2018).

xpd-9 B Anasori, C Shi, E Ju Moon, Y Xie, C Voigt, P Kent, S May, S Billinge, M Barsoum, Y Gogotsi, Control of Electronic Properties of 2D Carbides (MXenes) by Manipulating their Transition Metal Layers, *Nanoscale Horiz.*, **1**(3), 227-234 (2016).

xpd-10 P Urbankowski, B Anasori, K Hantanasirisakul, L Yang, L Zhang, B Haines, S May, S Billinge, Y Gogotsi, 2D Molybdenum and Vanadium Nitrides Synthesized by Ammoniation of 2D Transition Metal Carbides (MXenes), *Nanoscale*(45) (2017).

xpd-11 J Arinez-Soriano, J Jorge Albalad, A Carne-Sanchez, C Bonnet, F Busque, J Lorenzo, J Juanhuix, M Terban, I Imaz, et al., pH-Responsive Relaxometric Behaviour of Coordination Polymer Nanoparticles Made of a Gadolinium Macrocyclic Chelate, *Chem. Eur. J.*, **22**(37), 13162-13170 (2016).

xpd-12 A Beecher, O Semonin, J Skelton, J Frost, M Terban, H Zhai, A Alatas, J Owen, A Walsh, S Billinge, Direct Observation of Dynamic Symmetry Breaking above Room Temperature in Methylammonium Lead Iodide Perovskite, *ACS Energy Lett.*, **1**(4), 880-887 (2016).

xpd-13 S Masi, F Aiello, A Listorti, F Balzano, D Altamura, C Giannini, R Caliandro, G Uccello-Barretta, A Rizzo, S Colella, Connecting the Solution Chemistry of PbI 2 and MAI: A Cyclodextrin-Based Supramolecular Approach to the Formation of Hybrid Halide Perovskites, Chem. Sci., 9(12), 3200-3208 (2018).

xpd-14 S Colella, M Todaro, S Masi, A Listorti, D Altamura, R Caliandro, C Giannini, E Carignani, M Geppi, et al., Light-Induced Formation of Pb3+ Paramagnetic Species in Lead Halide Perovskites, ACS Energy Lett., 3, 1840-1847 (2018).

xpd-15 F Bertolotti, L Protesescu, M Kovalenko, S Yakunin, A Cervellino, S Billinge, M Terban, J Pedersen, N Masciocchi, et al., Coherent Nanotwins and Dynamic Disorder in Cesium Lead Halide Perovskite Nanocrystals, *ACS Nano*, **11**(4), 3819-3831 (2017).

xpd-16 Z Cai, Y Bi, E Hu, W Liu, N Dwarica, Y Tian, X Li, Y Kuang, Y Li, et al, Single-Crystalline Ultrathin Co3O4 Nanosheets with Massive Vacancy Defects for Enhanced Electrocatalysis, *Adv. Energy Mater.*, **8**, 1701694 (2017).

xpd-17 J Stein, M Steimle, M Terban, A Petrone, S Billinge, X Li, B Cossairt, Cation Exchange Induced Transformation of InP Magic-Sized Clusters, *Chem. Mater.*, **29**(18), 7984-7992 (2017).

xpd-18 M Terban, C Shi, R Silbernagel, A Clearfield, S Billinge, Local Environment of Terbium(III) Ions in Layered Nanocrystalline Zirconium(IV) Phosphonate–Phosphate Ion Exchange Materials, *Inorg. Chem.*, **56**, 8837-8846 (2017).

xpd-19 H Zhang, S Liu, M Scofield, S Wong, X Hong, V Prakapenka, E Greenberg, T Tyson, Structural Phase Transitions in SrTiO3 Nanoparticles, *Appl. Phys. Lett.*, **111**, 052904 (2017).

## 2. *Physics (ex situ structure)*

Electronic transport and electronic correlations closely depend on long-range ordering and/or local structural features, and drive the physical properties (magnetism, quantum Hall effect, conductivity, etc). XPD conducts a very active research in this domain. Examples are:

**Superconductivity**: The compound $IrTe_2$ is known to exhibit a transition to a modulated state featuring Ir-Ir dimers, with large associated atomic displacements[32]. Partial substitution of Pt or Rh for Ir destabilizes the modulated structure and induces superconductivity. PDF reveals that the local structure of $Ir_{0:95}Pt_{0:05}Te_2$ and $Ir_{0:8}Rh_{0:2}Te_2$ dichalcogenide superconductors with compositions just past the dimer/superconductor boundary is explained well by a dimer-free model down to 10 K, ruling out the existence of dimer nanoscale fluctuations [xpd-20].

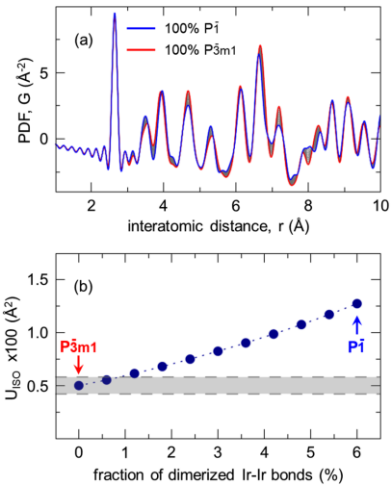


**Figure 22** [xpd-20]: Quantification of PDF sensitivity to the presence of dimers. (a) Simulated PDFs of IrTe2 comprising mixtures of dimer (*P*1) and non-dimer (*P*3*m*1) phases, with a mixing ratio increment of 0.1. The different solid profiles correspond to dimer fractions ranging from 6% of dimerized Ir-Ir nearest neighbors (as observed in the *P*1 phase, blue) to no dimers (which is the case for *P*3*m*1, red). PDFs for the intermediates are shown in gray. (b) Isotropic ADP of Ir obtained by fitting the dimer-free *P*3*m*1 model to the simulated PDFs in (a) as a function of absolute fraction of dimerized Ir-Ir bonds. The gray shaded region represents typical uncertainty on the 2$\sigma$ level in determining this parameter from the experimental PDFs using the same *P*3*m*1 model.

The iron-based superconductor $Sr_{1-x}Na_xFe_2As_2$ contains a magnetic phase with reentrant tetragonal symmetry. Structural refinements reveal local (~2 nm) orthorhombic fluctuations, despite the tetragonal symmetry of the average static structure [xpd-21].
The evolution of superconducting critical temperature Tc(x) in the 2H-$TaSe_2$−$xS_x$ alloy series correlates with the full width at half maximum of the Bragg peaks and with the linear term of the high-temperature resistivity. The charge density wave order is suppressed, and the superconductivity is maximized with crystallographic disorder [xpd-22].

**Magnetism**: the atomic and magnetic structures of the dilute ferromagnetic semiconductor system $(Ba,K)(Zn,Mn)_2As_2$ are using temperature-dependent x-ray and neutron PDF [xpd-23]. The average crystallographic structure retains its tetragonal structure at all temperatures, but the unit cell volume shows an anomaly at the ferromagnetic ordering temperature, consistent with volume

[32] G. L. Pascut, K. Haule, M. J. Gutmann, S. A. Barnett, A. Bombardi, S. Artyukhin, T. Birol, D. Vanderbilt, J. J. Yang, S.-W. Cheong, and V. Kiryukhin, Phys. Rev. Lett. 112, 086402 (2014)

magnetostriction. In addition, a well-defined local orthorhombic distortion with asymmetric displacements of the As and Zn/Mn atoms exists on a very short length scale of ≤5Å.

**Quantum materials**: $RENiO_3$ (RE ¼ rare-earth element) and $V_2O_3$ are archetypal Mott insulator systems. When tuned by chemical substitution ($RENiO_3$) or pressure ($V_2O_3$), they exhibit a quantum phase transition (QPT) between an antiferromagnetic Mott insulating state and a paramagnetic metallic state. The details of the Mott QPT are studied [xpd-24].
2-dimensional materials such as metal dichalcogenides (TMDs) $MX_2$ (M is a transition metal, X is a chalcogen atom), can be either semiconducting or semi-metallic[33]. The evidence for the low temperature orthorhombic structure in $MoTe_2$ is provided [xpd-25].

**Thermoelectricity**: the electronic structure, electric and thermal transport properties of $Ru_{1-x}IrxSe_2$ (x ≤ 0.2) are reported [xpd-26]. $RuSe_2$ is a semiconductor that crystallizes in a cubic pyrite unit cell. Ru0.8Ir0.2Se2 shows a semiconductor-metal crossover at about 30 K. This work indicates the importance of the electronic correlations in enhanced thermoelectricity of $RuSb_2$.

**Semiconductors**: Doping of nanocrystals (NC) is a key, yet under-explored, approach for tuning the electronic properties of semiconductors. An important route for doping of NCs is by vacancy formation. The size and concentration dependence of doping is studied in copper(I) sulfide ($Cu_2S$) NCs through a redox reaction with iodine molecules (I2). Vacancies are formed and diffraction reveals transformation from $Cu_2S$ to Cu-depleted phases and CuI formation [xpd-27].


xpd-20 R Yu, S Banerjee, H Lei, R Sinclair, M Abeykoon, H Zhou, C Petrovic, Z Guguchia, E Bozin, Absence of local fluctuating dimers in superconducting Ir1−x(Pt,Rh)xTe2, *Phys. Rev. B: Condens. Matter*, **97**, 174515 (2018).

xpd-21 B Frandsen, K Taddei, M Yi, A Frano, Z Guguchia, R Yu, Q Si, D Bugaris, R Stadel, R et al. Phys. Rev. Letters 119, 187001 (2017).

xpd-22 L Li, X Deng, Z Wang, Y Liu, M Abeykoon, E Dooryhee, A Tomic, Y Huang, J Warren, et al., Superconducting Order from Disorder in 2H-TaSe2-xSx, Quantum Materials **2**, 11 (2017).

xpd-23 B Frandsen, Z Gong, M Terban, S Banerjee, B Chen, C Jin, M Feygenson, Y Uemura, S Billinge, Local Atomic and Magnetic Structure of Dilute Magnetic Semiconductor (Ba,K)(Zn,Mn)2As2, *Phys. Rev. B: Condens. Matter*, **94**, 094102 (2016).

xpd-24 B Frandsen, L Liu, S Cheung, Z Guguchia, R Khasanov, E Morenzoni, T Munsie, A Hallas, M Wilson, et al. , Volume-wise Destruction of the Antiferromagnetic Mott Insulating State Through Quantum Tuning, *Nat. Commun.*, **7**, 12519 (2016).

xpd-25 Z Guguchia, F von Rohr, Z Shermadini, A Lee, S Banerjee, A Wieteska, C Marianetti, B Frandsen, H Luetkens, et al., Signatures of the topological s +− superconducting order parameter in the type-II Weyl semimetal Td-MoTe2, *Nat. Commun.*, **8**, 1082 (2017).

xpd-26 K Wang, A Wang, A Tomic, L Wang, A Abeykoon, E Dooryhee, S Billinge, C Petrovic, Enhanced Thermoelectric Power and Electronic Correlations in RuSe2, *APL Mater.*, **3**(4), 041513 (2015).

xpd-27 O Elimelech, J Liu, A Plonka, A Frenkel, U Banin, Size Dependence of Doping by a Vacancy Formation Reaction in Copper Sulfide Nanocrystals , *Angew. Chem. Int. Ed.*, **56**(35), 10335-10340 (2017).

xpd-28 A Wang, I Zaliznyak, W Ren, L Wu, D Graf, V Garlea, J Warren, E Bozin, Y Zhu, C Petrovic, Magnetotransport Study of Dirac Fermions in YbMnBi2 Antiferromagnet , *Phys. Rev. B: Condens. Matter*, **94**(16), 165161 (2016).

xpd-29 C Yang, Y Zhang, J Bai, B Qu, P Tong, M Wang, J Lin, R Zhang, H Tong, et al., Crossover of Thermal Expansion From Positive to Negative by Removing the Excess Fluorines in Cubic ReO3-type TiZrF7-x, *J. Mater. Chem. C*, **6**, 5148 (2018).

xpd-30 T Tyson, W Gao, Y Chen, S Ghose, Y Yan, Large Thermal Motion in Halide Perovskites, *Sci. Rep.*, **7**, 9401 (2017).


[33] Clarke, R., Marseglia, E. et al. A low-temperature structural phase transition in b-MoTe2. Philos. Mag. B 38, 121 (1978)

## 3. *Battery and Energy Storage Materials.*

### 3.1 Structure of battery materials and relationship with electrochemical performance

Lithium-ion batteries (LIBs) are still the object of active research to transition these systems from widely used portable electronics to large-scale applications such as electric vehicles (EV), hybrid electric vehicles (HEV) and clean, grid-scale electrical energy storage[34]. The battery rate capability, energy density, capacity fading and lifetime in operation are key metrics. Both high performance and low cost ($ per W.h) ultimately need to be achieved in order to replace fuel by electrical power and incentivize mass adoption of EVs and HEVs.

Layered transition metal oxide compounds (AMO , A = Li+ or Na+, M = transition metal ions) are important cathode materials for rechargeable Li-ion and Na-ion batteries, owing to their compact crystal structure, and thus have the ability to realize high energy density. Charge compensation of these compounds upon alkali ions (Li+ and Na+) intercalation/deintercalation is simultaneously balanced by reduction/oxidation of transition metal species (such as Mn, Co, and Ni). Although it is not a common phenomenon in layered oxide cathodes, oxygen anions may also participate in the charge compensation in addition to the cationic redox reactions[35]. The redox reaction on oxygen anions may cause reversible global crystal structure change as indicated by XRD measurement [xpd-31].

A very wide variety of battery materials is examined at XPD with emphasis on cathode variants of the conventional $LiCoO_2$ and $LiFePO_4$ cathode materials in commercial LIB technology: layered lithium nickel oxide [xpd-32]; Li- and Mn-rich (LMR) like $Li_2Ru_{0.5}Mn_{0.5}O_3$ [xpd-33]; vanadium pentoxide ($V_2O_5$) aerogel [xpd-34]; silver vanadate phosphate ($Ag_2VO_2PO_4$) [xpd-35]); copper ferrite ($CuFe_2O_4$) [xpd-36]; $LiZnFe_2O_4$ [xpd-37]. LMR cathode materials ($xLi_2MnO_3{\cdot}(1-x)LiMO_2$) for example can provide reversible capacities >280 mAh/g, where conventional Li-ion cathodes typically have capacities of 150-180 mAh/g [xpd-33].

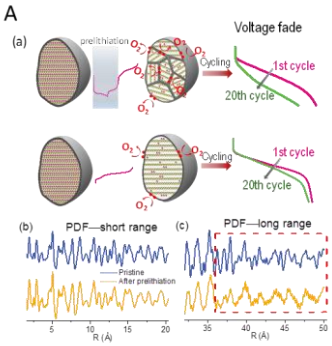


**Figure 23** [xpd-33]: explore the effects of microstructure defects on Voltage Fade of Li- and Mn-rich Cathodes.

However, LIBs are expensive due to the use of precious Li, Ni and Co metals, somewhat limiting their scalability for emerging EV, HEV and grid applications. The development of energy storage technologies based on environmentally abundant, low-toxicity materials is desirable.

α-$MnO_2$ materials are studied for electrochemical energy storage due the lower hazard of Manganese. Lithium doped sodium manganese oxide cathode materials, $Na_{0.6}Li_{0.2}Mn_{0.8}O_2$, show high initial capacity of ~223 mAh/g and excellent capacity retentions, attributed primarily to the absence of phase transformation in a wide potential range of electrochemical cycling [xpd-38]. A series of α-

[34] B. Kang, G. Ceder, *Nature* 2009, *458*, 190.

[35] Sathiya, M., Rousse, G., Ramesha, K., Laisa, C.P., Vezin, H., Sougrati, M.T., Doublet, M.L., Foix, D., Gonbeau, D., Walker, W., et al. (2013). Reversible anionic redox chemistry in high capacity layered-oxide electrodes. Nat. Mater. 12, 827–835.

$MnO_2$ samples (more specifically the 1D tunnel structured cryptomelane type manganese dioxide, $Mn_8O_{16}$) is studied at XPD to figure out the role of tunnel cation (K+) on the lithium ion electrochemistry of α-MnO2 cathode [xpd-39]. Surface treatment of α-$MnO_2$ with Ag+ ($Ag_2O$ additive) to form $Ag_{1.2}Mn_8O_{16}$ (silver hollandite) is shown to improve the electrochemistry, including a decreased charge-transfer resistance and higher deliverable energy density at a high rate [xpd-40].

**Figure 24** [xpd-2]: (a) Synchrotron NSLS-II XPD data and Rietveld refinement. (b) Voltage versus capacity of Li/AgxMn8O16 electrochemical cells. (c) Relative composition map calculated from EELS spectrum across L-Ag1.2Mn8O16 nanorod. (d) HAADF of H- Ag1.6Mn.

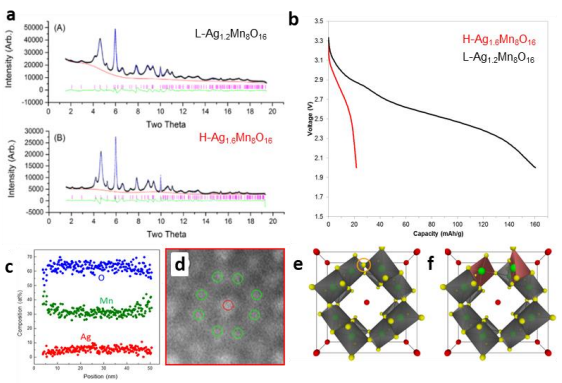


Hollandites (OMS-2) manganese oxides in general, are an intriguing class of sorbents, catalysts, and energy storage materials with a tunnel structure permitting one-dimensional insertion and de-insertion of ions and small molecules along the c direction[36]. The structure and defects of Ag hollandite nanorods are studied through the combined use of local (atomic imaging, electron diffraction, electron energy-loss spectroscopy) and bulk (synchrotron-based X-ray diffraction, thermogravimetric analysis) techniques [xpd-2, xpd-41].

Several XPD studies focus on alternative systems like all solid-state sodium ion batteries (SIBs) that benefit from the natural availability of sodium and the safer use of non-flammable organic electrolytes[37]: $Na_3SbSe_4$ [xpd-42]; $Na_3Ni_2BiO_6$ [xpd-43].

Magnesium-ion batteries (MIB) offer an opportunity for high volumetric capacity due to the di-cationic nature of Mg2+. However, the strong Mg2+-anion electrostatic attractions within the cathode lattice slows Mg2+ diffusion and exchange[38]. Thus, an important challenge is identification of cathodes capable of faster Mg2+ (de)insertion and of electrolytes that facilitate Mg2+ (de)solvation: spinel $MgMn_2O_4$ in organic Mg2+ electrolyte is studied [xpd-44].


xpd-2 L Wu, F Xu, Y Zhu, A Brady, J Huang, J Durham, E Dooryhee, A Marschilok, E Takeuchi, K Takeuchi, Structural Defects of Silver Hollandite, AgxMn8Oy, Nanorods: Dramatic Impact on Electrochemistry, *ACS Nano*, **9**(8), 8430-8439 (2015).

xpd-31 X Rong, J Liu, E Hu, Y Liu, Y Wang, J Wu, X Yu, K Page, Y Hu, et al., Structure-Induced Reversible Anionic Redox Activity in Na Layered Oxide Cathode. Joule **2**(1), 125-140 (2017).

xpd-32 J Xu, F Lin, D Nordlund, E Crumlin, F Wang, J Bai, M Doeff, W Tong, Elucidation of the Surface Characteristics and Electrochemistry of High-performance LiNiO2, *Chem. Commun.*, **52**, 4239-4242 (2016).

xpd-33 E Hu, Y Lyu, H Xin, J Liu, L Han, S Bak, J Bai, Y Yu, H Li, X Yang, Explore the Effects of Microstructural Defects on Voltage Fade of Li- and Mn-Rich Cathodes, *Nano Lett.*, **16**, 5999-6007 (2016).

xpd-34 L Wangoh, Y Huang, R Jezorek, A Kehoe, G Watson, F Omenya, N Quackenbush, N Chernova, M Whittingham, L Piper, Correlating Lithium Hydroxyl Accumulation with Capacity Retention in V2O5 aerogel cathodes, *ACS Appl. Mater. Interfaces*, **8**(18), 11532-11538 (2016).


[36] Li, L.; King, D. L. Synthesis and Characterization of Silver Hollandite and Its Application. Chem. Mater. 2005, 17, 4335.
[37] B. Dunn, H. Kamath, J.-M. Tarascon, Science 334 (2011) 928–935.
[38] N. N. Rajput, X. Qu, N. Sa, A. K. Burrell and K. A. Persson, J. Am. Chem. Soc., 2015, 137, 3411–3420.

xpd-35 R Zhang, T Abtew, N Quackenbush, L Wangoh, M Huie, A Brady, D Bock, H Efstathiadis, M Whittingham, et al., Electrode Reaction Mechanism of Ag2VO2PO4 Cathode, *Chem. Mater.*, **28**(10), 3428-3434 (2016).
xpd-36 C Cama, C Pelliccione, A Brady, J Li, E Stach, J Wang, E Takeuchi, K Takeuchi, A Marschilok, Redox Chemistry of a Binary Transition Metal Oxide (AB2O4): a Study of the Cu2+/Cu0 and Fe3+/Fe0 Interconversions Observed Upon Lithiation in a CuFe2O4 battery using X-ray Absorption Spectroscopy, *Phys. Chem. Chem. Phys.*, **18**, 16930-16940 (2016).
xpd-37 Y Zhang, C Pelliccione, A Brady, H Guo, P Smith, P Liu, A Marschilok, K Takeuchi, E Takeuchi, Probing the Li Insertion Mechanism of ZnFe2O4 in Li-Ion Batteries: A Combined X-Ray Diffraction, Extended X-Ray Absorption Fine Structure, and Density Functional Theory Study, *Chem. Mater.*, **29**(10), 4282-4292 (2017).
xpd-38 L Yang, X Li, X Ma, S Xiong, P Liu, Y Tang, S Cheng, Y Hu, M Liu, H Chen, Design of high-performance cathode materials with single-phase pathway for sodium ion batteries: A study on P2-Nax(LiyMn1-y)O2 compounds, *J. Power Sources* 381 (2018) 171-180.
xpd-39 A Poyraz, J Huang, C Pelliccione, X Tong, S Cheng, L Wu, Y Zhu, A Marschilok, K Takeuchi, E Takeuchi, Synthesis of Cryptomelane Type α-MnO2 (KxMn8O16) Cathode Materials with Tunable K+ Content: the Role of Tunnel Cation Concentration on Electrochemistry, *J. Mater. Chem. A*, **5**, 16914 (2017).
xpd-40 P Smith, A Brady, S Lee, A Bruck, E Dooryhee, L Wu, Y Z, K Takeuchi, E Takeuchi, A Marschilok, Deliberately Designed Atomic-Level Silver-Containing Interface Results in Improved Rate Capability and Utilization of Silver Hollandite for Lithium-Ion Storage, *ACS Appl. Mater. Interfaces*, **10**(1), 400-407 (2017).
xpd-41 A Brady, J Huang, J Durham, P Smith, J Bai, E Takeuchi, A Marschilok, K Takeuchi, The Effect of Silver Ion Occupancy on Hollandite Lattice Structure, MRS Advances, 3(10), 547-552 (2018).
xpd-42 S Xiong, Z Liu, H Rong, H Wang, M McDaniel, H Chen, Na3SbSe4−xSx as Sodium Superionic Conductors, *Sci. Rep.* 8 (2018) 9146.
xpd-43 J Liu, L Yin, L Wu, J Bai, S Bak, X Yu, Y Zhu, X Yang, P Khalifah, Quantification of Honeycomb Number-Type Stacking Faults: Application to Na3Ni2BiO6 Cathodes for Na-Ion Batteries, *Inorg. Chem.*, **55**(17), 8478-8492 (2016).
xpd-44 J Yin, A Brady, E Takeuchi, A Marschilok, K Takeuchi, Magnesium-ion Battery-relevant Electrochemistry of MgMn2O4: Crystallite Size Effects and the Notable Role of Electrolyte Water Content, *Chem. Commun.*, **53**(26), 3665-3668 (2017).

## 3.2 Structural transformations operando

In order to improve the performance of existing electrochemical energy storage systems or to guide material design for the next generation devices, one needs to reveal how the structural, chemical, and morphological electrode/electrolyte materials evolve during operation.

XPD excels at delivering a high flux, high-energy x-ray beam for operando diffraction. XPD enables such studies as LIB cycling, to understand correlations between transition-metal chemistry, structure, and lithium storage electrochemical behavior as in high capacity lithium-rich layered compounds: $LiNi_{1/3}Mn_{1/3}Co_{1/3}O_2$ (NMC) [xpd-45] and $Li_2Ru_{0.5}Mn_{0.5}O_3$ [xpd-46].

A variety of optimization strategies includes using electrode materials composed of nano-particles, surface coatings and/or additives to reduce ion diffusion length and increase electronic conductivity[39]. For example, the lithium-sulfur battery exhibits superior theoretical energy density of 2,600Wh/kg, which surpasses that of current state-of-the-art LIBs with typical energy density of 300–600Wh/kg[40]. However, metal sulfide additives like CuS may cause undesired parasitic reactions. Operando diffraction, as a function of depth of discharge, is an unsurpassed tool to monitor the dissolution of the additive in the electrolyte, the

[39] J. J. Wang, J. Yang, Y. Tang, J. Liu, Y. Zhang, G. Liang, M. Gauthier, Y. K. Chen-Wiegart et al., *Nat. Commun.* 2014, *5*, 3415.
[40] Manthiram, A., Fu, Y. Z., Chung, et al, Y. S. Rechargeable Lithium-Sulfur Batteries. *Chem Rev* **114**, 11751–11787 (2014).

formation of intermediate polysulfide species and the end products—$Li_2S$ and sulfur—whose low electrical conductivity results in poor cycling performance and limited active-material utilization [xpd-47].

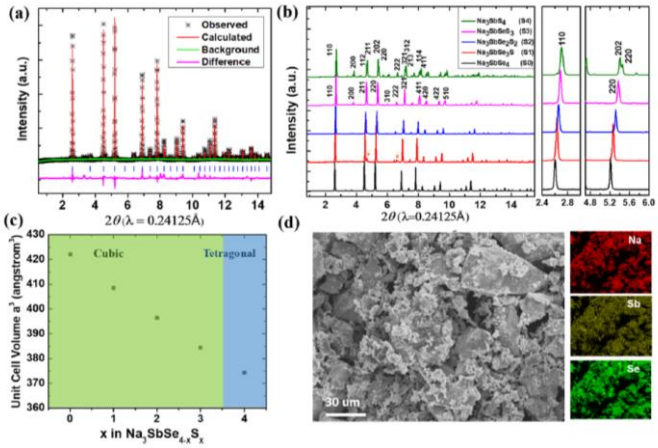


**Figure 25** [xpd-47]: (a) XRD pattern of Na3SbSe4 and the Rietveld refinement. (b) XRD patterns of Na3SbSe4−*x*S*x*. (Minor impurities of NaSbSe2 in S1 are labeled with arrows). (c) Cell volume variation with respect to S concentration in Na3SbSe4−*x*S*x*. (d) SEM images of as-synthesized Na3SbSe4 and corresponding EDX mapping of Na3SbSe4.

Current LIB cathodes such as $LiCoO_2$, $LiFePO_4$, or $LiNi_xMn_yCo_{1-x-y}O_2$ are exclusively based on intercalation mechanism, which involves topotactic intercalation/deintercalation of Li+ in a host lattice. However, the LIB cathodes have specific capacities that range only between 140 and 200 mAh/g, which limit their energy densities[41]. Alternatively, certain metallic oxide, sulfide, or halide compounds can experience conversion reactions with Li+ by accepting multiple electrons per formula, delivering much higher capacities. Among them, a high-performance $Fe_{0.9}Co_{0.1}OF$ cathode material, with high energy density of ~1,000 Wh/kg and long cycle life. Its phase evolution is analyzed during (de)lithiation [xpd-48]. The lithiation/de-lithiation mechanism in systems like silver ferrite-based batteries ($AgFeO_2$ and $Ag_{0.2}FeO_{1.6}$) is investigated using ex situ, *in situ*, and operando XPD techniques [xpd-49].


xpd-45 Y Zhou, J Yue, E Hu, H Li, L Gu, K Nam, S Bak, X Yu, J Liu, et al, High-Rate Charging Induced Intermediate Phases and Structural Changes of Layer-Structured Cathode for Lithium-Ion Batteries, *Adv. Energy Mater.*, **6** (2016) 1600597.

xpd-46 Y Lyu, E Hu, D Xiao, Y Wang, X Yu, G Xu, S Ehrlich, K Amine, L Gu, et al., Correlations between Transition Metal Chemistry, Local Structure and Global Structure in Li2Ru0.5Mn0.5O3 Investigated in a Wide Voltage Window, *Chem. Mater.*, **29**(21), 9053-9065 (2017).

xpd-47 K Sun, C Zhao, C Lin, E Stavitski, G Williams, J Bai, E Dooryhee, K Attenkofer, J Thieme, et al., Operando Multi-modal Synchrotron Investigation for Structural and Chemical Evolution of Cupric Sulfide (CuS) Additive in Li-S battery, *Sci. Rep.*, **7**(1), 12976 (2017).

xpd-48 X Fan, E Hu, Y Zhou, F Han, S Hwang, J Liu, S Bak, Z Ma, T Gao, S Liou, High energy-density and reversibility of iron fluoride cathode enabled via an intercalation-extrusion reaction, *Nat. Commun.*, **9**(1), 2324 (2018).

xpd-49 J Durham, A Brady, C Cama, D Bock, C Pelliccione, Q Zhang, M Ge, H Yan, X Huang, et al., Electrochemical (de)lithiation of Silver Ferrite and Composites: Mechanistic Insights From Ex Situ, In Situ, and Operando X-ray Techniques, *Phys. Chem. Chem. Phys.*, **19**, 22329-22343 (2017).


[41] Whittingham, M. S. Ultimate limits to intercalation reactions for lithium batteries. Chem. Rev. 114, 11414–11443 (2014)

## 3.3 *in situ* synthesis of battery materials

Preparing stoichiometric Ni-rich $LiNi_{1-x}M_xO_2$ cathode materials with ordered layer structure and high reversible capacity, proves difficult due to cation mixing in octahedral sites[42]. *In situ* studies of synthesis reactions of LiNiO2 and the Co-substituted variant, $LiNi_{0.8}Co_{0.2}O_2$ are carried out [xpd-50]. Direct transformation from the rock salt phase to a Li-deficient layered phase, followed by a gradual structural ordering process during heat treatment. Co substitution facilitate the nucleation of a Co-rich layered phase at low temperatures and subsequent growth and stabilization of a solid solution $Li(Ni,Co)O_2$ upon further heat treatment.

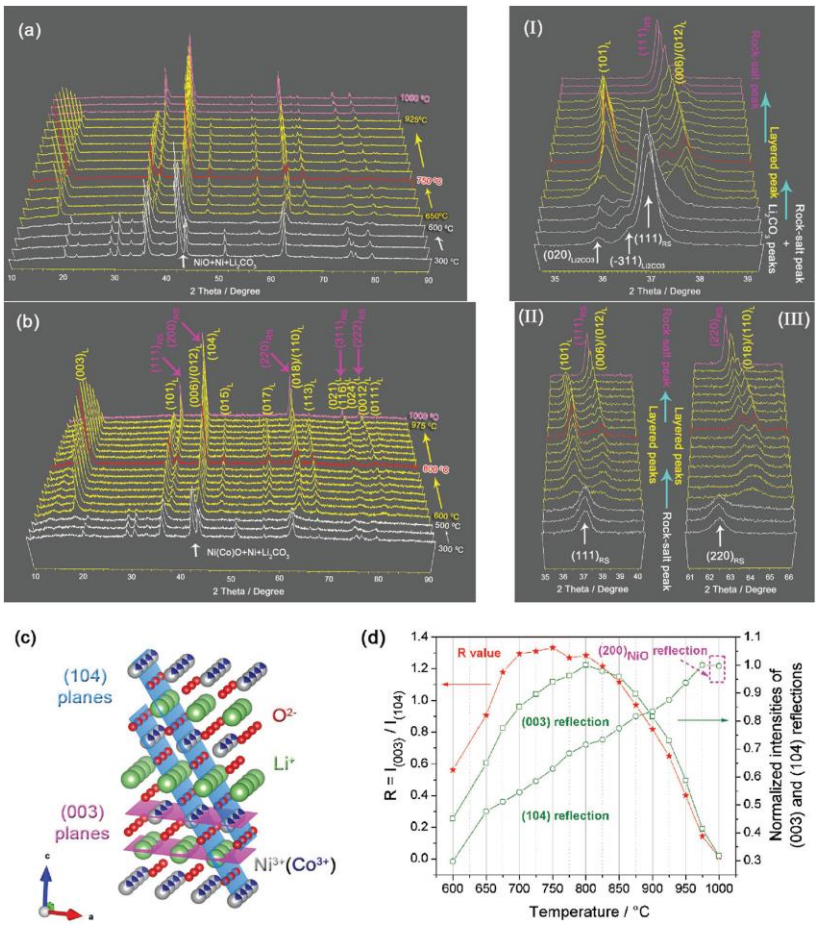


**Figure 26** [xpd-50]: In situ tracking structural evolution of the intermediates during solid-state synthesis of Ni-rich oxides in O2 flow. a,b) In situ XRD patterns recorded during synthesis of LiNiO2 and LiNi0.8Co0.2O2, respectively, along with enlarged 2θ portions, (I) between 35° and 39° from (a), (II, III) between 35°–40° and 61°–66° from (b), indicating a direct transition from the initial rock salt into the layered phase (as illustrated). c) Illustration of the atomic configure and reflection planes of (104) and (003) in the layered structure, indicating the high sensitivity of the (003) reflection to the cationic ordering (i.e., occupancies of Li, Ni, and Co ions), in contrast to the independence of (104) on the ordering. d) Evolution of the intensity of (003) and (104) reflections during synthesis of LiNi0.8Co0.2O2 (green circles and squares, respectively, with lines as a guide to the eye), and the ratio of the two, *R* = *I*(003)/*I*(104) (red stars with the line as a guide to the eye); the values were extracted from in situ XRD patterns in (b).

Total scattering and absorption spectroscopy are employed to track the long-/short-range structural evolution and, locally, the oxidation of all constituent TM cations in $TMO_6$ octahedra during the synthesis of $LiNi_{0.77}Mn_{0.13}Co_{0.10}O_2$ from hydroxide precursors ($Ni_{0.77}Mn_{0.13}Co_{0.10}(OH)_2$) [xpd-4]. High-Ni transition metal layered oxides are potential cathode materials for LIBs whose electrochemical activity is largely determined by the cationic ordering in octahedra.

[42] W. Liu, P. Oh, X. Liu, M.-J. Lee, W. Cho, S. Chae, Y. Kim, J. Cho, Angew. Chem. Int. Ed. 2015, 54, 4440

xpd-4 Zhang, Ming-Jian; Teng, Gaofeng; Chen-Wiegart, Yu-chen; Duan, Yandong; Ko, Jun Young; Zheng, Jiaxin; Thieme, Juergen ; Dooryhee, Eric; Chen, Zonghai; Bai, Jianming; Amine, Khalil; Pan, Feng; Wang, Feng. Cationic Ordering Coupled to Reconstruction of Basic Building Units during Synthesis of High-Ni Layered Oxides. J. Am. Chem. Soc. (2018).

xpd-50 J Zhao, W Zhang, A Huq, S Misture, B Zhang, S Guo, L Wu, Y Zhu, Z Chen, et al., In Situ Probing and Synthetic Control of Cationic Ordering in Ni-Rich Layered Oxide Cathodes, *Adv. Energy Mater.*, **7**(3), 1601266 (2016).

## 4. *Synthesis (in situ)*

The lack of a mechanistic framework for chemical reactions forming inorganic extended solids presents a challenge to accelerated materials discovery[43]. *In situ* X-ray diffraction measurements is used to monitor solid-state reactions and deduce reaction pathways, while theoretical computations rationalize reaction energetics. The method is applied to the $La_2CuO_4$–$xS_x$ ($0 \leq x \leq 4$) quaternary system, following an earlier prediction that enhanced superconductivity could be found in these new lanthanum copper(II) oxysulfide compounds [xpd-3]. In this particular *in situ* reaction, reactants containing Cu(II) and S(2−) ions undergo redox reactions, leaving their ions in oxidation states that are incompatible with forming the desired new compounds.

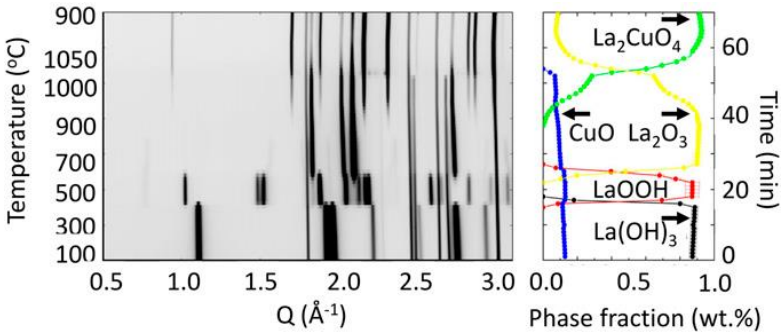


**Figure 27** [xpd-3]: Synthesis of La2CuO4 from La2O3 and CuO powders, monitored by in situ powder XRD. At Left is shown the evolution of the diffraction peaks as temperature changes, and at Right is shown the weight fraction of each phase determined from Rietveld refinements of the diffraction patterns.

During *in situ* synthesis of a prototypical MOF, ZIF-8, synchrotron X-ray PDF analysis is sensitive to dilute species, and complemented by mass spectrometry, electron microscopy, and density functional theory calculations [xpd-51]. Despite rapid formation of the crystalline product, a high concentration of $Zn(2\text{-MeIm})_4$ (2-MeIm = 2-methylimidazolate) initially forms and persists as stable clusters over long times. A secondary, amorphous phase also pervades during the synthesis, which has a structural similarity to the final ZIF-8 and may act as an intermediate to the final product.

Compared to conventional high temperature (>500°C) furnace-based synthesis, Micro-Wave Radiation (MWR) assisted synthesis (0.3–300 GHz) is a novel method for rapid, single-step, low temperature (<200°C) synthesis of mixed ordered-disordered materials for potential use in photocatalysis, thermoelectrics, or lithium ion batteries[44]. Experiments at XPD demonstrate <u>for the first time</u> that ceramic oxide films of titanium dioxide ($TiO_2$) grown with MWR contain

[43] Shoemaker DP, et al. (2014) In situ studies of a platform for metastable inorganic crystal growth and materials discovery. Proc Natl Acad Sci USA 111:10922–10927

[44] S. Komarneni, R. Roy and Q. H. Li, Mater. Res. Bull., 1992, 27, 1393–1405.

a different phase composition and increased crystallinity compared to $TiO_2$ grown at similar temperatures without EM fields [xpd-52]. Specifically, field-assisted $TiO_2$ is composed of a mixed-phase structure consisting of long-range anatase $TiO_2$ phase with short-range amorphous components. In contrast, furnace-grown materials are amorphous with local ordering most resembling the brookite phase of $TiO_2$.

Other in-situ experiments are done on a variety of materials:

- Metal–semiconductor hybrid nanoparticles[45] (NPs): time-resolved diffraction follows the formation of Au–InAs core–shell NCs composed of a crystalline Au core and a disordered porous shell [xpd-53].
- Lanthanide (Ln)-doped upconverting nanocrystals (UCNCs), such as $NaLnF_4$ (with Ln = lanthanide): results reveal a complex mechanism of the formation of $NaGdF_4$:Yb:Er UCNCs based on chemical reactions involving molecular clusters [xpd-54].

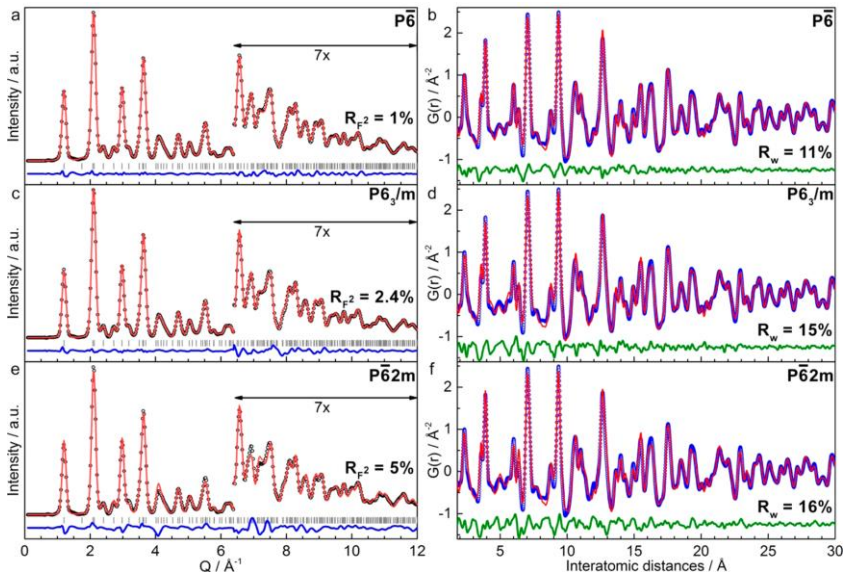


**Figure 28** [xpd-54]: Structure refinement results of the as-prepared β-NaGdF4:Yb:Er UCNCs based on bulk crystal structures related to space groups: P6̄(a,b), P63/m (c,d), and P6̄2m (e,f). The left and right columns show the results obtained by the Rietveld and PDF analyses, respectively. For Rietveld analyses (i.e., left column), the black circles represent the experimental XPD (X-ray powder diffraction) pattern, the red lines the modeled XPD patterns, and the blue lines (shifted for clarity) the difference between experimental and modeled XPD patterns. Bragg peak positions are indicated by gray tick marks. For PDF analyses (i.e., right column), the blue circles represent the experimental PDF, the red lines the modeled PDFs, and the green lines (shifted for clarity) the difference between experimental and modeled PDFs. For all Rietveld and PDF analyses, the goodness of fit is indicated (bottom-right). Note that within a column, all graphics have been plotted with the same scales for the x and y axes so that direct visual juxtapositions (especially regarding the difference curves) are possible

.

[45] Banin, U.; Ben-Shahar, Y.; Vinokurov, K. Hybrid Semiconductor–Metal Nanoparticles: From Architecture to Function. Chem. Mater. 2014, 26, 97−110

xpd-3 H He, C Yee, D McNally, J Simonson, S Zellman, M Klemm, P Kamenov, G Geschwind, A Zebro, S Ghose, Combined Computational and Experimental Investigation of the La2CuO4–xSx *Proc Natl Acad Sci USA, **115**(31), 7890-7895 (2018).*

xpd-51 M Terban, D Banerjee, S Ghose, B Medasani, A Shukla, B Legg, Y Zhou, Z Zhu, M Sushko, et al., Early stage structural development of prototypical zeolitic imidozolate framework (ZIF) in solution, *Nanoscale*, **10**, 4291-4300 (2018).

xpd-52 N Nakamura, M Terban, S Billinge, B Reeja-Jayan, Unlocking the Structure of Mixed Amorphous-crystalline Ceramic Oxide Films Synthesized Under Low Temperature Electromagnetic Excitation, *J. Mater. Chem. A*, **5**, 18434 (2017).

xpd-53 J Liu, Y Amit, Y Li, A Plonka, S Ghose, L Zhang, E Sach, U Banin, A Frenkel, Reversed Nanoscale Kirkendall Effect in Au–InAs Hybrid Nanoparticles, *Chem. Mater.*, **28**, 8032-8043 (2016).

xpd-54 D Hudry, A Abeykoon, E Dooryhee, D Nykypanchuk, J Dickerson, Probing the Crystal Structure and Formation Mechanism of Lanthanide-Doped Upconverting Nanocrystals, *Chem. Mater.*, **28**(23), 8752-8763 (2016).

## *5. Materials Processing*

Field assisted sintering techniques employ electrical fields and currents in combination with temperature and pressure, to reduce sintering times and temperatures[46]. Flash sintering (FS), is a type of field assisted sintering[47], that has predominantly been applied to ceramic materials, with phenomenal rates of densification at remarkably low temperatures[48].

FS consists in applying a modest electric field across the sample[49]. Stage I of FS is the incubation time which precedes the flash event, that is characterized by the onset of a rapid, nonlinear increase in the current (current runaway) flowing through the specimen under constant applied voltage. In stage II, the current is limited by switching the power supply to current control. In stage III, the specimen is held in a constant state of flash under current control.

A lot of effort has been invested at XPD to enable flash sintering of various materials:

- Uranium oxide, a common nuclear fuel ($UO_2$ and $U_4O_9$). Stoichiometry and FS parameters can be tailored to optimize the fabrication process for nuclear fuels [xpd-55].
- Titanium oxide ($TiO_2$) where atomic displacements measured by PDF <u>for the first time</u> are found to be far greater for oxygen atoms than for titanium atoms. This may signal an “elastic softening” of the lattice, which recently has been predicted as a precursor to the onset of flash [xpd-56]
- FS treatment of MgO and $\alpha$-$Al_2O_3$ is studied in [xpd-57]

xpd-55 D Sprouster, E Kardoulaki, R Weidner, A Raftery, M Elbakhshwan, R Pokharel, H Reiche, D Byler, S Ghose, et al., In situ X-ray characterization of uranium dioxide during flash sintering Materialia 00 (2018) 1-7.

xpd-56 B Yoon, D Yadav, R Raj, S Ghose, P Sarin, D Shoemaker, Measurement of O and Ti atom displacements in TiO2 during flash sintering experiments, *J. Am. Ceram. Soc.*, **101**(5), 1811-1817 (2017). [203349]

xpd-57 B Yoon, D Yadav, S Ghose, R Raj, Reactive flash sintering: MgO and $\alpha$-$Al_2O_3$ transform and sinter into single-phase polycrystals of $MgAl_2O_4$, *J. Am. Ceram. Soc.* (2018).

[46] C.E.J. Dancer, Mater. Res. Express 3 (2016) 102001

[47] J.S.C. Francis , R. Raj , J. Am. Ceram. Soc. 95 (2012) 138

[48] M. Biesuz, W.D. Abate, V.M. Sglavo, J. Am. Ceram. Soc. 101 (2018) 71

[49] Cologna M, Rashkova B, Raj R. Flash sintering of nanograin zirconia in<5 s at 850°C. J Am Ceram Soc. 2010;93:3556-3559

The efficiency of turbine-based, steam mediated power generation is predominantly limited by the maximum service temperature of exposed steel components[50]. To this end, advances in the fabrication of creep-resistant, high-strength steels[51] have resulted in alloys capable of long-term structural stability to temperatures as high as 973K. Protective coatings are used to inure exposed components to corrosion, wear, and oxidation under consistently harsh operating conditions[52]. The stability and thermal expansion rate of a chromium aluminide, as a potential material for high-temperature protective coating, are studied at XPD [xpd-58].

xpd-58 R Rosa, S Bhattacharya, J Pabla, H He, J Misuraca, Y Nakajima, A Bender, A Antonacci, W Adrip, et al., Pseudo-icosahedral Cr55Al232−δ as a high-temperature protective material, *Phys. Rev. Materials*, **2**, 032401 (2018).

## *6. Nuclear Science*

Synchrotron based X-ray methods have become increasingly important to probe the (micro)structure, morphology, chemistry and structural evolution of nuclear materials[53]. Diffraction can help characterize and identify those nuclear materials that are resilient in aggressively corrosive and oxidizing environments. XPD, with its high-energy x-ray beam and robotic arm for manipulating radioactive materials, is a perfect host for these studies. The adaptation of the XPD beamline to work on radioactive materials is described in [xpd-59].

**Reactor Pressure Vessel (RPV) Steels**: massive, thick-walled pressure vessels are permanent nuclear reactor structures that are exposed to a damaging flux of neutrons from the adjacent core. The neutrons cause embrittlement of the RPV steel that grows with dose (fluence), as manifested by an increasing ductile-to-brittle fracture transition temperature[54]. Extending reactor lifetime requires demonstrating that large safety margins against brittle fracture are maintained at the higher neutron fluence associated with beyond 60 years of service. XRD and SAXS are used to characterize highly embrittling nm-scale Mn–Ni–Si precipitates that develop in the RPV irradiated steels at high fluence [xpd-60]. These precipitates lead to severe embrittlement that is not accounted for in current regulatory models.

**Silicon Carbides**: SiC based materials display novel structural properties including resistance to radiation damage, high specific strength and retention of this strength at high temperatures[55]. SiC is studied as a potential structural material in advanced reactors (fission and fusion), and as an accident tolerant fuel cladding for light water reactors[56]. Several neutron fluence- and irradiation temperature-dependent changes in the microstructure of SiC are shown [xpd-61].

[50] R. J. Campbell, Congressional Research Service Report No. 7-5700, 2013, https://fas.org/sgp/crs/misc/R42923.pdf
[51] S.-H. Kim, H. Kim, and N. J. Kim, Nature (London) 518, 77 (2015)
[52] S. Tang, S. Zhu, X. Tang, H. Pan, X. Chen, and Z. D. Xiang, Corros. Sci. 80, 374 (2014)
[53] A. Bonnin, J.P. Wright, R. Tucoulou, H. Palancher, Appl. Phys. Lett. 105 (2014) 084103
[54] G.R. Odette, B.D. Wirth, D.J. Bacon, N.M. Ghoniem, MRS Bull. 26 (2001) 176
[55] L.L. Snead, T. Nozawa, Y. Katoh, T. Byun, S. Kondo, D.A. Petti, J. Nucl. Mater. 371 (2007) 329
[56] Y. Katoh, K. Ozawa, C. Shih, T. Nozawa, R.J. Shinavski, A. Hasegawa, L.L. Snead, J. Nucl. Mater. 448 (2014) 448

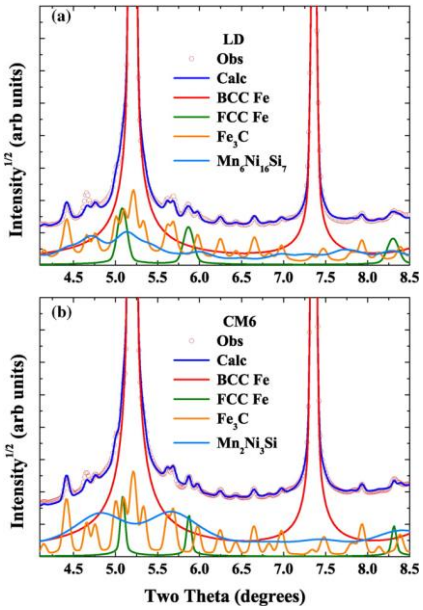


**Figure 29** [xpd-60]: Modified Rietveld refinements for the (a) LD and (b) CM6 irradiated samples. The components of each phase are included for reference. The magnified range highlights the broad features of the small MNSP component(s). The blue curve identifies the MNSP structures

**Amorphous Fe-alloy**: nanostructured and amorphous materials are expected to exhibit radiation resistance stemming from their inherent lack of long range order that offers free volume for migration and localization or elimination of radiation-induced defects. The effects of temperature and spallation-induced neutron irradiation on amorphous Fe-alloy nanostructured coatings on alloy steel substrates are studied at XPD [xpd-62]. Ductility is essentially preserved following radiation with modest neutron doses of ~$2 \times 10^{18}$ n/cm$^2$. At higher neutron doses of ~$2 \times 10^{19}$ n/cm$^2$, the material experiences radiation-induced embrittlement that adversely results in ductility loss.

**High Entropy Alloys (HEA)**: PDF (combined with TEM, Atom Probe Tomography and DFT) is used to study the local structure of the face-centered cubic (fcc) FeCoNiCr MEA, and FeCoNiCrMn and FeCoNiCrPd HEAs before and after ion irradiation. The local lattice distortions are quantitatively evaluated based on the difference of lattice constant between the local structure (PDF low R-range, first atomic shell) and the average structure (PDF high R-range) [xpd-63].


xpd-59 D Sprouster, S Ghose, T Novakowski, P Wells, G Odette, R Weidner, E Dooryhee, T Stan, N Almirall, L Ecker, Infrastructure development for radioactive materials at the NSLS-II, *Nucl. Instrum. Meth. A*, **880** (2017). [203327]

xpd-60 D Sprouster, J Sinsheimer, E Dooryhee, S Ghose, P Wells, T Stan, N Almirall, G Odette, L Ecker, Structural Characterization of Nanoscale Intermetallic Precipitates in Highly Neutron Irradiated Reactor Pressure Vessel Steels, *Scripta Mater.*, **113**(1), 18-22 (2015).

xpd-61 D Sprouster, T Koyanagi, E Dooryhee, S Ghose, Y Katoh, L Ecker, Microstructural Evolution of Neutron Irradiated 3C-SiC, *Scripta Mater.*, **137**, 132-136 (2017).

xpd-62 N Simos, Z Zhong, E Dooryhee, S Ghose, S Gill, F Camino, I Savklryildiz, E Akdogan, Neutron irradiation and high temperature effects on amorphous Fe-based nano-coatings on steel - A macroscopic assessment, *J. Nucl. Mat.*, **489**, 164-179 (2017).

xpd-63 Y. Tong, G. Velisa, S. Zhao, W. Guo, T. Yang, K. Jin, C. Lu, H. Bei, J. Ko, et al., Evolution of local lattice distortion under irradiation in medium- and high-entropy alloys, Materialia **0**, 1-9 (2018).

# 7. *Instrumentation, Detectors, Methods*

## 7.1 Detectors

An inherent limitation in medical imaging performance using flat panel detectors is the depth-dependence in the spatial response of scintillators to X-rays; light produced by each X-ray interaction spreads laterally in a scintillator before it is collected, and the spatial extent of these light bursts varies with interaction depth (Fig. 30). This phenomenon degrades and fundamentally limits the spatial frequency-dependent detective quantum efficiency[57]. The work at XPD is the first experimental measurements of the depth-dependent modulation transfer function of thallium-doped cesium iodide (CsI) and terbium-doped $Gd_2O_2S$ (GOS) scintillators with thickness ranging from 200–1000µm [xpd-64, xpd-65, xpd-66].

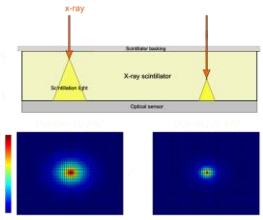


**Figure 30** [xpd-64]: Depth-dependent spatial response of scintillators


xpd-64 A Howansky, A Lubinsky, S Ghose, K Suzuki, W Zhao, Direct Measurement of Lubberts effect in CsI:Tl scintillators using single x-ray photon imaging, *SPIE Medical Imaging 2017*, Vol 10132, sponsored by SPIE (2017).

xpd-65 A Howansky, A Lubinsky, S Ghose, K Suzuki, W Zhao, Investigation of random gain variations in columnar CsI: Tl using single x-ray photon imaging, *SPIE Medical Imaging 2018*, Vol 10573, p. 105730, sponsored by SPIE (2018).

xpd-66 A Howansky, A Lubinsky, K Suzuki, S Ghose, W Zhao, An apparatus and method for directly measuring the depth-dependent gain and spatial resolution of turbid scintillators, *Med. Phys.*, (2018).


## 7.2 Methods

The characterization of thin films has so far been limited by the need for grazing-incidence techniques. In some cases, the film can be isolated from the substrate and standard characterization techniques can be used, but most often this is not possible due to the small mass of sample present as film. tfPDF thus opens the way for many new possibilities in materials characterization for thin films as demonstrated for the first time in the case of the $FeSb_x$ samples [xpd-67]. PDFs are obtained from supported thin film samples at XPD, using normal-incidence X-ray diffraction measurements. The use of XPD's high-flux, high-energy X-rays and careful background subtraction in Q-space make it possible to obtain a clear scattering signal from amorphous, nanocrystalline and polycrystalline films down to a thickness of at least a few hundred nanometers


xpd-67 K Jensen, A Blichfeld, S Bauers, S Wood, E Dooryhee, D Johnson, B Iversen, S Billinge, Demonstration of Thin Film Pair Distribution Function Analysis (tfPDF) for the Study of Local Structure in Amorphous and Crystalline Thin Films, *IUCrJ*, **2**, 481-489 (2015).

xpd-68 A Colli, K Attenkofer, B Raghothamachar, M Dudley, Synchrotron X-Ray Topography for Encapsulation Stress/Strain and Crack Detection in Crystalline Silicon Modules, *IEEE J. Photovoltaics*, **6**(5), 1387-1389 (2016).


[57] G. Lubberts, "Random Noise Produced by X-Ray Fluorescent Screens" J. Optical Society of America, 58(11), 1475 (1968)

### 7.3 Sample Environments

See appendix 3

xpd-69 M Elbakhshwan, S Gill, A Motta, R Weidner, T Anderson, L Ecker, Sample Environment for in situ Synchrotron Corrosion Studies of Materials in Extreme Environments, *Rev. Sci. Instrum.*, **87**(10), 105122 (2016).

## *8. Sorption studies*

XPD is well suited for looking at kinematics and static structure of sorption. Two cases are published, that only partly reflect the effort in this field.

Chemical warfare agents (CWAs) continue to present a significant threat in the event of war or terrorist attacks[58]. The new generation of sorptive or catalytically active materials for CWA decontamination includes metal organic frameworks. A detailed study of the adsorption and decomposition of a nerve-agent simulant, dimethyl methylphosphonate (DMMP), in several MOFs uses SR-based X-ray powder diffraction, X-ray absorption, and infrared spectroscopy [xpd-70].

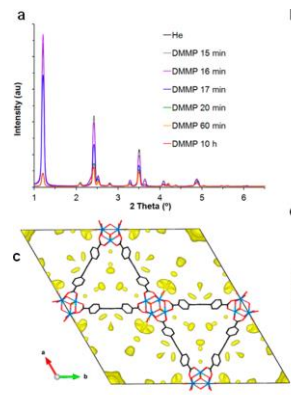


**Figure 31** [xpd-70]: (a) In situ PXRD data of NU-1000 collected during the exposure to DMMP. (c) Difference Fourier electron density map of DMMPtreated NU-1000 after 10 h. Zr = blue, C = black, and O = red. Hydrogen atoms have been removed for clarity. Electron density iso-surface is drawn at 0.3 ē/Å3 in yellow.

MOFs can be employed for capturing radioactive iodine formed upon fission of nuclear fuel[59]. Raman and optical electronic spectroscopy in combination with powder X-ray diffraction are used to probe the electronic structure of iodine in MOFs as a function of pressure (DAC cell, up to 8GPa, 300K) [xpd-71]. One type of MOF shows polymerization of iodine molecules into a 1D polyiodide chain inside the straight channels of the MOF. In the second type, iodine in the sinusoidal channels retains its molecular (I2) character. This study illustrates adaptations of the electronic structure of iodine to channel topology and strength of the iodine-framework interaction.

Unstable isotopes of Xe and Kr are produced in the fission of uranium and plutonium. Separating low concentration of Xe from its sister noble gas Kr in air is an important step in removing radioactive gases from spent nuclear fuels. In 2010, the DOE requested that a BNL-led team research the possibility of using a getter material like nanostructured MOFs.

[58] Yang, Y. C.; Baker, J. A.; Ward, J. R. Chem. Rev. 1992, 92, 1729

[59] Soelberg, N. R.; Garn, T. G.; Greenhalgh, M. R.; Law, J. D.; Jubin, R.; Strachan, D. M.; Thallapally, P. K. Radioactive Iodine and Krypton Control for Nuclear Fuel Reprocessing Facilities. Sci. Technol. Nucl. Install. 2013, 2013, 1–12

The operando opportunities of NSLS-II for catalysis science are shown in [xpd-72].


xpd-70 A Plonka, Q Wang, W Gordon, A Balboa, D Troya, W Guo, C Sharp, S Senanayake, J Morris, et al., In Situ Probes of Capture and Decomposition of Chemical Warfare Agent Simulants by Zr-Based Metal Organic Frameworks, *J. Am. Chem. Soc.*, **139**(2), 599-602 (2017).

xpd-71 S Lobanov, J Daly, A Goncharov, X Chan, S Ghose, H zhong, L Ehm, T Kim, J Parise, Iodine in Metal-organic Frameworks at High Pressure, *J. Phys. Chem. A*, **122**, 6109-6117 (2018)

xpd-72 R Palomino, E Stavitski, I Waluyo, Y Chen-Wiegart, M Abeykoon, J Sadowski, J Rodriguez, A Frenkel, S Senanayake, New In-Situ and Operando Facilities for Catalysis Science at NSLS-II: The Deployment of Real-Time, Chemical, and Structure-Sensitive X-ray Probes, *Synch. Rad. News*, **30**(2), 30-37 (2017).


## *9. Earth Science*

In situ XRD is used to determine the microstructural evolution and particle orientation of raw clays (kaolin) between freezing (−10°C) and temperatures below boiling (90°C). Three parameters are considered to explain the effect of temperature on clay microstructure: the clay particle orientation, pore size distribution, and pore connectivity [xpd-73].


xpd-73 K Jaradat, Z Darbari, M Elbakhshwan, S Abdelaziz, S Gill, E Dooryhee, L Ecker, Heating-freezing Effects on the Orientation of Kaolin Clay Particles, *Appl. Clay Sci.*, **150**, 163-174 (2017).

# Appendix 2 – Beamline Staff

**Table 7: XPD Beamline Staff**

| | | |
|---|---|---|
| Eric Dooryhee | Beamline lead | |
| Sanjit Ghose | Beamline scientist | |
| Jianming Bai | Science Associate | |
| John Trunk | Technical Coordinator<br>(matrixed across all beamlines of the DISC program) | |
| John Parise | BNL-Stony Brook Joint Appointee | |
| Lars Ehm | BNL-Stony Brook Joint Appointee | |

# Appendix 3 – Sample Environment

**Table 8: Sample Environments**

| | | |
|---|---|---|
| Lamp furnace | RT- 1800°C, XRD only with user-supplied capillaries | 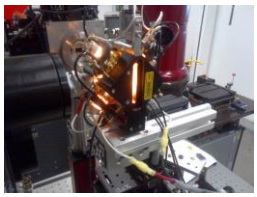 |
| Flat Plate furnace (®Linkam) | RT- 1500°C | 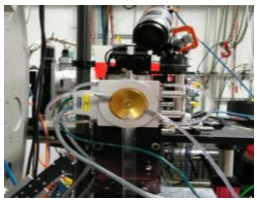 |
| DSC/XRD heating unit (®Linkam) | -196°C to 600°C<br>Coll. J. Parise and L. Ehm, Stony Brook | |
| Hot Air Blower (®FMB-Oxford) | RT- 1000°C | |
| Cryostream (®FMB-Oxford) | 80K-500K | 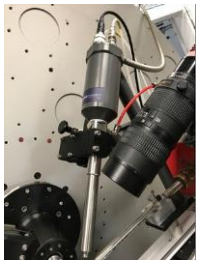 |
| He cryostat (Cryo Industries of America) | 10K-500K | |
| Corrosion Cell [xpd-69] | 400°C, 1500psi<br>Coll. S. Gill, BNL | |

| | | |
|---|---|---|
| Liquid Flow Reactors | Multiple solvents with syringe pump | 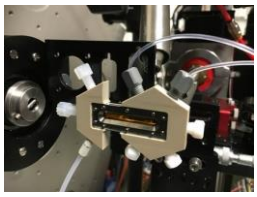 |
| Gas Flow cell furnace | Coil heater RT to 800°C<br>gas flow at about 10 mL/min . Allowed gas type: He, Ar etc. | 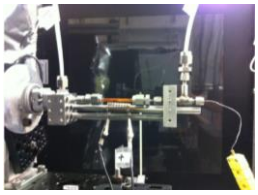 |
| Multi-purpose Cell | oxidative/corrosive gases, 3D stress, vertical and axial loads up to 20lbs<br>Coll. N. Simos, BNL | 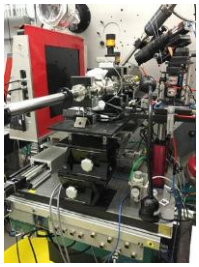 |
| High Pressure Reaction Cell | High pressure system with syringe pump (max 150bar) and manifold for user-custom cells and a simple cell with Kapton capillary(Max pressure 100bar) | 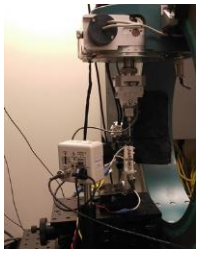 |
| Microwave Furnace (Muegge GmbH) | 2.3-2.5GHz, tunable power<br>Coll. R. Jayan,<br>Carnegie Mellon University | 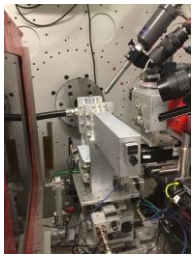 |
| Vertical Resistive Heater | RT- 650°C | |
| triaxial cell | ≤5MPa, -20°C to 90°C<br>Coll. S. Abdelaziz, BNL | 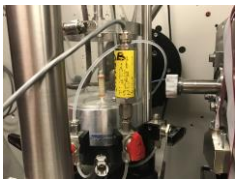 |

| | | |
|---|---|---|
| Gas-Handling System | includes gas racks, gas cabinets, mass flow controllers, bubblers, sensors and safeguards. The non-hazardous gases are He, $N_2$, $O_2$, $CO_2$, Ar, Kr, Xe and mixes; the hazardous gases include $H_2$, CO, $CH_4$, $C_2H_4$, NO, $NO_2$, $SO_2$, and $CH_3S_x$. Gas lines feed through wall and roof labyrinths into the lead-shielded hutches. | |

The XPD beamline uses laboratory 1LL09 designed for miscellaneous manipulation and mounting of powder and/or single crystal samples. Equipment includes:

- Mettler AX205 Analytical Semi Micro Balance (81-220 g range, 0.01 mg accuracy)
- Wild Heerbrugg M5A Stereo microscope
- Cole-Parmer ultrasonic bath
- Fisher micro centrifuge (Model 235A)
- Forced-air oven by Lab Safety (Model 32EZ27, max temperature 250°C, +/- 1°C stability)
- Corning hot plate stirrer (model PC351)
- Tektronix TAS 455 two-channel Oscilloscope
- Agilent 33220A 20 Mhz waveform generator
- Beltron UV lamp (250W)
- High-pressure syringe pump (TeleDyne 500D, 700bar)
- Small self-contained torch for sealing capillaries
- Lead soldering station
- Milli-Q IQ 7000 water purifier
- Orbital shaker
- A variety of lab tools *e.g*. tweezers, spatulas, cutters, agate mortar and pestle, glassware, double-sided tape, Kapton film/tape, gloves, kimwipes, pipets, copper and aluminum foils, and Kapton/glass capillary containers.
- The lab has a HEPA filtered fume hood for wet chemistry with exposure control (Air Sentry).

# Appendix 4 – User partnership

The respective PU's contributions are detailed here:

1. S. Billinge – University of Columbia - BNL:
    a. build software for instrument control, data acquisition and on-line visualization and processing (coll. with DAMA; see documentation on GitHub and XPD beamline wiki web site)
    b. build effective capabilities for XPD and PDF beamlines that include: detection scheme optimization, new sample holders, thin film transmission PDF methodology, high throughput and combinatorial approaches, space-resolved scanning technique incl. XRD/PDF CT-tomography
    c. help to develop and support the high-energy science user-community at XPD and PDF beamlines.

PU agreement is expiring end of 2018. A new PUA is being discussed for the next 3 years, with a requested 9% user beamtime set aside and to be distributed between the XPD (28-ID-2) and PDF (28-ID-1) beamlines depending on need and availability.

2. L. Ecker – BNL - National Scientific User Facility (NSUF, Idaho National Laboratory):
    a. XPD endstation 2 XRD/PDF CT-tomography equipment (funded by DOE-NE) that is described in Fig. 14, including the control system for 72 axes and 3D reconstruction and visualization software
    b. Maintenance of the PU contributed equipment during the term of the PU Agreement including repairs of any damage that occurs during their standard and approved use.
    c. Technical and science commissioning of the PU-contributed equipment to meet the NSLS-II requirements for general user operations. Expect start of commissioning end of 2018.
    d. Scientific and technical staffing for providing direct operational and user support on the PU-contributed equipment.

The 3-year PU agreement started October 2017.

3. D. Weidner - Consortium for Materials Properties Research in Earth Sciences (COMPRES) – Stony Brook University:
    a. Complete Large Volume Press set-up in XPD endstation 2, that includes a ®Perkin-Elmer a-Si flat panel XRD detector, large volume press with hydraulics, WC and sintered diamond anvils, cell assemblies, optical imaging setup with camera and optical components, motion control with precision stages & tables, control and analysis computers with software licenses
    b. Preparation laboratory tools, microscopes, and consumables made available for all users of the above equipment
    c. Maintenance of the PU contributed equipment during the term of the PU Agreement including repairs of any damage that occurs during their standard and approved use.
    d. Technical and science commissioning of the PU-contributed equipment to meet the NSLS-II requirements for general user operations

e. Scientific and technical staffing for providing direct operational and user support on the PU-contributed equipment.

PU agreement is under review. Expected start of General User operations is 2018-3.

# 2018 SAC Review of the NSLS-II Beamlines

**Wednesday and Thursday, September 19-20, 2018**
**Brookhaven National Laboratory, Upton, NY 11973, USA**

As part of the NSLS-II Science Advisory Committee (SAC) charter, the SAC will conduct periodic reviews of the NSLS-II beamline programs, typically every 3-5 years. The purpose of these reviews is to help the facility to assess the scientific utilization, output, and impact of the beamlines, their long-term programmatic directions and associated user communities, the operation effectiveness the beamlines, and the processes relevant to user access and support at the beamlines.

For a newly operating beamline, NSLS-II plans to conduct the first SAC review when the beamline is in or already completed its third year of general user operations. This first review is intended to be informative, provide constructive feedback on progress to-date, guidance on ways to improve, and suggestions of possible new directions to pursue. The reviews are also an excellent opportunity for the beamline staff to self-reflect on their achievements and to layout the vision for the upcoming years.

NSLS-II will hold the first such SAC Review of NSLS-II Beamlines on **Wednesday and Thursday, September 19-20, 2018**. The scope of this 1½-day review will cover the first set of four beamlines: Coherent Soft X-ray Scattering (CSX, 23-ID-1), In-situ and Operando Soft X-ray Spectroscopy (IOS, 23-ID-2), X-ray Powder Diffraction (XPD, 28-ID-2), and Hard X-ray Nanoprobe (HXN, 3-ID), with each beamline reviewed by a separate SAC Beamline Review Committee.

The review committee is asked to evaluate and address the following charge questions:

- Beamline Capabilities: Are the beamline capabilities well established and supported to meet the research needs of the intended scientific communities? Are these well aligned with NSLS-II strengths and strategic directions? Are there opportunities to enhance the existing program or pursue new capabilities?
- Science Program and Impact: Is the current science program mix appropriate for the beamline? Is staff research at the appropriate level and aligned with the mission of the beamline? Is each science program productive and making sufficient impact in its scientific field? Are there potential efficiencies to be gained in scheduling, programmatic balance, or other ways to enhance productivity and impact?
- User Support and Labs: Is the user support at the beamline of high quality and sufficient to enable and sustain high productivity and high impact? Are there opportunities to improve user productivity? Are the support labs available and sufficiently equipped to enable the type of research at the beamline?
- Partner Users: For beamlines with partner users, are the partner users productive and making sufficiently high impact on the beamline science programs? Are the partner users contributing as planned, fulfilling their responsibilities, and satisfied with the partnership? Are there opportunities to further improve the existing partnerships or to pursue new partnerships that would enhance beamline operations and productivity?
- Future Plans: Is there an appropriate level of future planning at the beamline? Are these future plans appropriate given the current and evolving research trends in the community and funding climate? What other improvements and/or upgrades should be considered in the future?

NSLS-II will provide the relevant documents and presentations to the review committee, either before or at the review meeting. Please contact Tammy Stein (tstein@bnl.gov) if additional information is needed.

The review committee will make a short close-out report to the NSLS-II management and the SAC at the end of the review meeting. A final, written report should be submitted to the NSLS-II Director within 30 days of the review.